Astronomy & Astrophysics

Unveiling [C II] clumps in a lensed star-forming galaxy at *z* ∼ 3.4

A. Zanella[1], E. Iani[2], M. Dessauges-Zavadsky[3], J. Richard[4], C. De Breuck[5], J. Vernet[5], M. Kohandel[6],
F. Arrigoni Battaia[7], A. Bolamperti[8,1,5], F. Calura[9], C.-C. Chen[10], T. Devereaux[8], A. Ferrara[6],
V. Mainieri[5], A. Pallottini[6], G. Rodighiero[8], L. Vallini[9], and E. Vanzella[9]

[1] Istituto Nazionale di Astrofisica (INAF), Vicolo dell'Osservatorio 5, 35122 Padova, Italy
    e-mail: anita.zanella@inaf.it
[2] Kapteyn Astronomical Institute, University of Groningen, 9700 AV Groningen, The Netherlands
[3] Département d'Astronomie, Université de Genève, Chemin Pegasi 51, 1290 Versoix, Switzerland
[4] Univ. Lyon, Univ. Lyon1, ENS de Lyon, CNRS, Centre de Recherche Astrophysique de Lyon UMR5574,
    69230 Saint-Genis-Laval, France
[5] European Southern Observatory, Karl Schwarzschild Strasse 2, 85748 Garching, Germany
[6] Scuola Normale Superiore, Piazza dei Cavalieri 7, 56126 Pisa, Italy
[7] Max-Planck-Institut fur Astrophysik, Karl-Schwarzschild-Str 1, 85748 Garching bei Munchen, Germany
[8] Dipartimento di Fisica e Astronomia, Università degli Studi di Padova, Vicolo dell'Osservatorio 3, 35122 Padova, Italy
[9] INAF – Osservatorio Astronomico di Bologna, Via Gobetti 93/3, 40129 Bologna, Italy
[10] Academia Sinica Institute of Astronomy and Astrophysics (ASIAA), No. 1, Sec. 4, Roosevelt Road, Taipei 10617, Taiwan

ABSTRACT

Context. Observations at UV and optical wavelengths have revealed that galaxies at $z \sim 1-4$ host star-forming regions, dubbed "clumps", which are believed to form due to the fragmentation of gravitationally unstable, gas-rich disks. However, the detection of the parent molecular clouds that give birth to such clumps is still possible only in a minority of galaxies, mostly at $z \sim 1$.

Aims. We investigated the [C II] and dust morphology of a $z \sim 3.4$ lensed galaxy hosting four clumps detected in the UV continuum. We aimed to observe the [C II] emission of individual clumps that, unlike the UV, is not affected by dust extinction, to probe their nature and cold gas content.

Methods. We conducted ALMA observations probing scales down to ∼300 pc and detected three [C II] clumps. One (dubbed "NE") coincides with the brightest UV clump, while the other two ("SW" and "C") are not detected in the UV continuum. We do not detect the dust continuum.

Results. We converted the [C II] luminosity of individual clumps into molecular gas mass and found $M_{\rm mol} \sim 10^8\,M_\odot$. By complementing it with the star formation rate (SFR) estimate from the UV continuum, we estimated the gas depletion time ($t_{\rm dep}$) of clumps and investigated their location in the Schmidt–Kennicutt plane. While the NE clump has a very short $t_{\rm dep} = 0.16\,{\rm Gyr}$, which is comparable with high-redshift starbursts, the SW and C clumps instead have longer $t_{\rm dep} > 0.65\,{\rm Gyr}$ and are likely probing the initial phases of star formation. The lack of dust continuum detection is consistent with the blue UV continuum slope estimated for this galaxy ($\beta \sim -2.5$) and it indicates that dust inhomogeneities do not significantly affect the detection of UV clumps in this target.

Conclusions. We pushed the observation of the cold gas content of individual clumps up to $z \sim 3.4$ and showed that the [C II] line emission is a promising tracer of molecular clouds at high redshift, allowing the detection of clumps with a large range of depletion times.

Key words. galaxies: evolution – galaxies: formation – galaxies: high-redshift – galaxies: ISM – galaxies: structure

1. Introduction

In the last decades, rest-frame ultraviolet (UV) and optical observations have shown that star-forming galaxies at redshift $z \sim 1-4$ have irregular morphologies (e.g., Conselice et al. 2004; Conselice 2014; Shibuya et al. 2016; Huertas-Company et al. 2024), dominated by active sites of star formation, dubbed "clumps" (e.g., Elmegreen & Elmegreen 2005; Elmegreen et al. 2008; Förster Schreiber et al. 2011; Guo et al. 2015; Zanella et al. 2015). Spatially resolved observations taken with ground-based adaptive optics facilities (e.g., SINFONI on the Very Large Telescope, VLT), the *Hubble* Space Telescope (HST), and more recently the *James Webb* Space Telescope (JWST), revealed that clumps typically have stellar masses $M_\star \sim 10^7-10^9\,M_\odot$, star formation rates (SFRs) $\sim 0.1-10\,M_\odot\,{\rm yr}^{-1}$, and mostly unresolved sizes <1 kpc (e.g.,

Förster Schreiber et al. 2011; Guo et al. 2018; Zanella et al. 2019; Kalita et al. 2024). By combining the angular resolution of state-of-the-art telescopes with strong lensing, it has been possible to study clumps in the low-mass and low-SFR regime (Livermore et al. 2015; Vanzella et al. 2017a,b, 2021; Cava et al. 2018). Such studies have revealed that when magnification (and hence spatial resolution and sensitivity) increases, clumps with smaller sizes are uncovered (Vanzella et al. 2022; Meštrić et al. 2022; Claeyssens et al. 2023; Messa et al. 2022). In particular, clumps in lensed galaxies have effective radii $R_{\rm e} \sim 10-100\,{\rm pc}$, stellar masses $M_\star \sim 10^6-10^8\,M_\odot$, and SFRs $\sim 0.01-10\,M_\odot\,{\rm yr}^{-1}$ (Meštrić et al. 2022; Claeyssens et al. 2023). They have blue UV continuum β slopes, in several cases approaching extreme values ($\beta \sim -3$), indicating that they are active sites of star formation hosting young stellar populations with relatively low metallicity (Bolamperti et al. 2023). Observational evidence suggests that

the majority of $z \sim 1-4$ clumps have likely originated in situ in galaxies' disk (Shibuya et al. 2016; Zanella et al. 2019), supporting simulation results showing that clumps form due to disk instabilities in gas-rich galaxies (Bournaud et al. 2014; Ceverino et al. 2015; Tamburello et al. 2015; Mandelker et al. 2017; Leung et al. 2020; Zanella et al. 2021). If this scenario is indeed correct, we should also detect the parent molecular clouds that give birth to the clumps.

The molecular hydrogen (H_2), the fuel for star formation, is not directly observable at high redshift and carbon monoxide (CO) is typically used as a molecular gas tracer instead. CO in local star-forming galaxies is organized in giant molecular clouds (GMCs), with typical sizes $\sim 5-100$ pc and masses $M_{H2} \sim 10^4-10^7 \, M_\odot$ (Bolatto et al. 2013; Miville-Deschênes et al. 2017; Freeman et al. 2017). Spatially resolved observations of the CO emission in $z \sim 1-3$ star-forming galaxies instead are still sparse. Simulations predict the CO(5−4) transition to be the brightest in clumps at $z \sim 1-4$ due to their reservoir of warm, dense gas (Bournaud et al. 2015). Observations have been performed in a clumpy galaxy at $z \sim 1.5$ (Cibinel et al. 2015) and CO(5−4) has been detected from the nuclear region, coincident with a red, proto-bulge component. No detection has been found at the location of the star-forming clumps instead. This might be due to physical reasons, such as the short gas depletion timescale of clumps (Cibinel et al. 2015). In addition, observational limitations might be at play, such as the relatively coarse resolution of the observations (~ 1 kpc) and the lack of sufficient sensitivity. In addition, to overcome the lack of spatial resolution and sensitivity, mostly bright submillimeter galaxies (SMGs) lensed by foreground galaxy clusters have been targeted with the Atacama Large Millimeter/submillimiter Array (ALMA) to detect the dust-continuum, CO, or [C II] line emission of individual high-redshift clumps. Most of these works led to tentative or non-detections, or morphologies consistent with homogeneous dust and gas distributions (Gullberg et al. 2015, 2018; Hodge et al. 2016, 2019; Cañameras et al. 2017; Tadaki et al. 2018; Rujopakarn et al. 2019; Ivison et al. 2020; Ushio et al. 2021; Calura et al. 2021; Liu et al. 2023). However, since rest-frame UV observations of such SMGs are not available, it is unclear whether these targets are clumpy in the first place. The first robust detections of the CO(4−3) emission from individual clouds have been obtained in two clumpy, main-sequence galaxies at $z \sim 1$, lensed by foreground galaxy clusters, the Cosmic Snake (Dessauges-Zavadsky et al. 2019) and A521 (Dessauges-Zavadsky et al. 2023). Thanks to the combination of high-resolution observations ($\lesssim 0.2''$) and lensing magnification, tens of GMCs with sizes $\sim 30-200$ pc have been identified. They have molecular gas masses 100 times higher than local GMCs and ten times higher molecular gas surface densities ($\Sigma_{gas} \sim 10^3-10^4 \, M_\odot \, pc^{-2}$, Dessauges-Zavadsky et al. 2023). The GMCs in the Cosmic Snake and A521 show a spatial offset with respect to the clumps detected at rest-frame UV wavelengths, possibly indicating that GMCs are quickly disrupted (tens of millions of years) or dispersed after the first episode of star formation (Dessauges-Zavadsky et al. 2023), similarly to local GMCs that have typical lifetimes of $\sim 10-30$ Myr (Kruijssen et al. 2019; Chevance et al. 2020; Kim et al. 2021).

To detect the gas reservoir of young clumps, we targeted a $z \sim 3.4$ galaxy lensed by the foreground cluster Abell 2895, hosting four UV-bright clumps. High-resolution observations were carried out with ALMA targeting the [C II] $\lambda 158 \, \mu m$ emission line. This far-infrared (far-IR) fine-structure line is one of the main coolants of the interstellar medium (ISM, Stacey et al. 1991; Graciá-Carpio et al. 2011; Carilli & Walter 2013) and it

Table 1. Log of the ALMA observations.

ID	A2895a
Date	10 Oct. 2019
t_{exp}	1.9 h
Noise rms	0.03 mJy beam^{-1}
Beam	$0.31'' \times 0.26''$
Observed frequency range	418–434 GHz

Notes. Rows: (1) Galaxy ID; (2) Date of observations; (3) Integration time on source; (4) Noise rms of the continuum, estimated over a bandwidth of 4811 km s^{-1}; (5) FWHM of the beam.

has been often considered as a SFR tracer (De Looze et al. 2010, 2014; Capak et al. 2015). However, in recent years, there has been increasing observational evidence that [C II] is tightly correlated with the molecular gas (Zanella et al. 2018; Madden et al. 2020; Dessauges-Zavadsky et al. 2020; Gururajan et al. 2023), also supported by theoretical works and simulations (Pallottini et al. 2017a; Ferrara et al. 2019; Sommovigo et al. 2021; Vizgan et al. 2022). In this work we discuss the morphological analysis of the cold ISM of our lensed, clumpy target, determine the gas reservoir of individual clumps traced by [C II] and, thanks to complementary UV continuum observations tracing clumps' SFR, we estimate their gas depletion time.

This paper is organized as follows: in Sect. 2, we describe our target galaxy and the data set; in Sect. 3, we discuss how we obtained the [C II] and dust continuum maps and spectra, we describe the morphology of the galaxy as determined by considering different tracers and the detection of individual clumps; in Sect. 4, we discuss the physical properties (molecular gas mass, star formation rate, star formation efficiency) that we derived for our target; in Sect. 5, we report scaling relations among observables and place them in the context of current literature findings; finally, in Sect. 6, we conclude and summarize our findings. Throughout the paper we adopt a flat ΛCDM cosmology with $\Omega_M = 0.3$, $\Omega_\Lambda = 0.7$, and $H_0 = 70$ km s^{-1} Mpc^{-1}. All magnitudes are AB magnitudes (Oke 1974) and we adopt a (Chabrier 2003) initial mass function, unless differently stated.

2. Data

2.1. Our target galaxy and ancillary data

Our target is a clumpy galaxy lensed by the foreground brightest central galaxy (BCG) of the cluster Abell 2895. Three multiple images (M1, M2, and M3) have been identified and analyzed in previous studies (Livermore et al. 2015; Iani et al. 2021). However, only two of them are included in the ALMA primary beam (Table 1 and Sect. 2.3), hence in the following we only focus on M1 (RA = 01:18:11.184, Dec = −26:58:03.826) and M2 (RA = 01:18:10.851, Dec = −26:58:07.608; Fig. 1). The average lensing magnification of M1 and M2 is $\mu = 5.5 \pm 0.7$ and $\mu = 4.5 \pm 0.3$, respectively (Sect. 2.2, Livermore et al. 2015; Iani et al. 2021).

Our target has a redshift $z_{opt} = 3.39535 \pm 0.00025$, as estimated from optical emission lines (Iani et al. 2021) and the morphology of both its UV continuum and optical line (Hβ, [O III]) emission is clumpy. At least four star-forming clumps are detected on top of the diffuse emission, likely coming from the underlying disk (Fig. 1). Individual clumps have stellar masses $M_\star \lesssim 2 \times 10^8 \, M_\odot$ and effective radii, as measured from their

UV continuum emission, $R_e \lesssim 250\,pc$ (magnification corrected, Iani et al. 2021).

We complement our ALMA observations with a suite of ancillary data and a lensing model (Sect. 2.2). The rest-frame UV HST imaging has $FWHM \sim 0.13''$ resolution, while the VLT/SINFONI spectra targeting Hβ and [O III] are seeing limited ($FWHM \sim 0.6''$). The VLT/MUSE observations taken with the Adaptive Optics (AO) Wide Field Mode (WFM) and targeting the Lyα emission have $FWHM \sim 0.4''$ resolution. The peak of the Lyα emission is spatially offset with respect to the UV continuum and the optical emission lines (Iani et al. 2021). Such offset between the optical emission, which is co-spatial with the clumps, and the Lyα emission seems to indicate the presence of dust and/or neutral gas that absorb and scatter the Lyα. This offset is not due to astrometry issues, as the UV continuum from MUSE and HST data are co-spatial, and the HST astrometry is calibrated against *Gaia* DR3 (Iani et al. 2021).

2.2. Lensing model

The lensing model used in this work is discussed in detail in Iani et al. (2021). In brief, we used a mass model constructed using the Lenstool[1] software (Jullo et al. 2007), following the methodology described in Richard et al. (2010). The large-scale and cluster structure 2D-projected mass distributions are modeled, respectively, as a parametric combination of a cluster-scale and multiple galaxy-scale double pseudo-isothermal elliptical potentials (Elíasdóttir et al. 2007). The centers and shapes of the galaxy-scale components are constrained to the centroid, ellipticity and position angle of cluster members as measured on the HST image, to limit the number of parameters in the model. The cluster members are selected through the color–magnitude diagram method (e.g. Richard et al. 2014) and we assume that they follow the Faber–Jackson relation for elliptical galaxies (Faber & Jackson 1976). This model is constrained by using the location of our target and that of another triply imaged system with spectroscopic redshift $z \sim 3.7$ (Livermore et al. 2015; Iani et al. 2023). The best-fit model reproduces the location of the multiply imaged systems with a root-mean-square (rms) of $0.09''$. With Lenstool we produce a 2D map of the magnification factor at the redshift of our target, we resample the magnification maps to match the spatial sampling of our data, and we reconstruct the multiple images on the source plane (Fig. 1). This is done by using our lens model to raytrace back each spaxel, effectively subtracting the lensing displacement.

2.3. ALMA data

We carried out ALMA Band 8 observations for our target galaxy during Cycle 7 (PI: E. Iani, Project ID: 2019.1.01676.S) with the goal of detecting the [C II] emission line, one of the brightest far-infrared cooling lines (rest-frame frequency $\nu_{rf} = 1905.1\,GHz$), and possibly the underlying continuum. The dust continuum at these frequencies ($\nu_{obs} = 420-430\,GHz$) provides direct information about the dust-obscured SFR.

We observed our target for 1.9 h on source and reached a continuum sensitivity of $0.03\,mJy\,beam^{-1}$, over a bandwidth of $4811\,km\,s^{-1}$, and a sensitivity of $0.20\,mJy\,beam^{-1}$, over a bandwidth of $102\,km\,s^{-1}$, corresponding to the velocity width encompassed by the [C II] emission (Sect. 3.3). The native spectral resolution of the observations is 1.129 MHz ($\sim 0.78\,km\,s^{-1}$), later binned to lower velocity resolution ($\sim 20.3\,km\,s^{-1}$) to

achieve sufficient S/N for our purposes. The imaged beam size (natural weighting) is $FWHM = 0.31'' \times 0.26''$ (Table 1). We reduced the data with the standard ALMA pipeline, based on the CASA software, version 5.6.1 (McMullin et al. 2007). The quasar J2258−2758 was chosen as the flux and bandpass calibrator. We then converted the calibrated datacubes to *uvfits* format and analyzed them with the software GILDAS (Guilloteau & Lucas 2000). We did not perform continuum subtraction, as the continuum of our target is not detected (see Sect. 3.2).

3. Analysis

3.1. Modeling the UV continuum 2D light profile

We fit the UV continuum emission of our target by using GAL-FIT (Peng et al. 2002, 2010). The process we adopted is fully detailed in Iani et al. (2021), but we briefly summarize it in the following. We created a median PSF by stacking the non-saturated stars detected in the HST field of view. We subtracted the BCG 2D light profile by fitting it with two Sérsic models, convolved with the PSF. We then modeled the 2D surface brightness of our target with a 2D Sérsic profile (the galaxy "diffuse" component) and subtracted the best-fit model from the data to obtain a "residuals" map. In the residuals we identified four clumps. We ran again GALFIT including additional parametric models to fit the clumps, namely two Sérsic profiles for the clumps with larger diameter than the FWHM of the PSF and two PSF profiles for clumps that are spatially unresolved. Adopting Gaussian profiles instead of PSFs to model the clumps yields consistent results; however, we prefer to adopt PSF profiles to limit the number of free parameters of the fit. To estimate the intrinsic (magnification-corrected) flux of individual clumps, we divided the observed HST image by the amplification map (Sect. 2.2) to obtain pixel-by-pixel corrected fluxes. We then fit the 2D light distribution of the galaxy with the best-fit model, letting the normalization (magnitude) of each component free to fit the data. Given that the magnification is fairly uniform for our target, we instead estimated the magnification-corrected effective radii of the marginally resolved clumps by dividing their observed effective radius (as derived by GALFIT) by the square-root of the average magnification factor at the location of the clump. The best-fit parameters are reported in Table 2. We repeated this analysis independently on M2 and reached consistent conclusions.

In Fig. 2, we show the best-fit model and the residuals obtained by subtracting the model from the data for M1 and M2. The residuals are consistent with noise fluctuations and the center of the Sérsic profile associated with the galaxy "diffuse" component is consistent ($<0.2''$ difference) with the barycenter estimated with SExtractor (Bertin & Arnouts 1996). To check the robustness of our estimate of the UV barycenter, we also smoothed the HST data to the angular resolution of the ALMA data, by convolving them with a Gaussian kernel. The clumps are less prominent, but the UV emission still appears less spatially extended than the [C II]. We estimated the barycenter of the UV emission by fitting the smoothed data with a single Sérsic profile. Once again, the barycenter coordinates are consistent with those obtained with SExtractor (Fig. 2). In the following, we refer to the UV barycenter as the one derived with SExtractor.

3.2. Continuum emission map

We created averaged continuum maps by integrating the spectral range, after excluding the channels where the flux is dominated

---

[1] https://projects.lam.fr/projects/lenstool/wiki
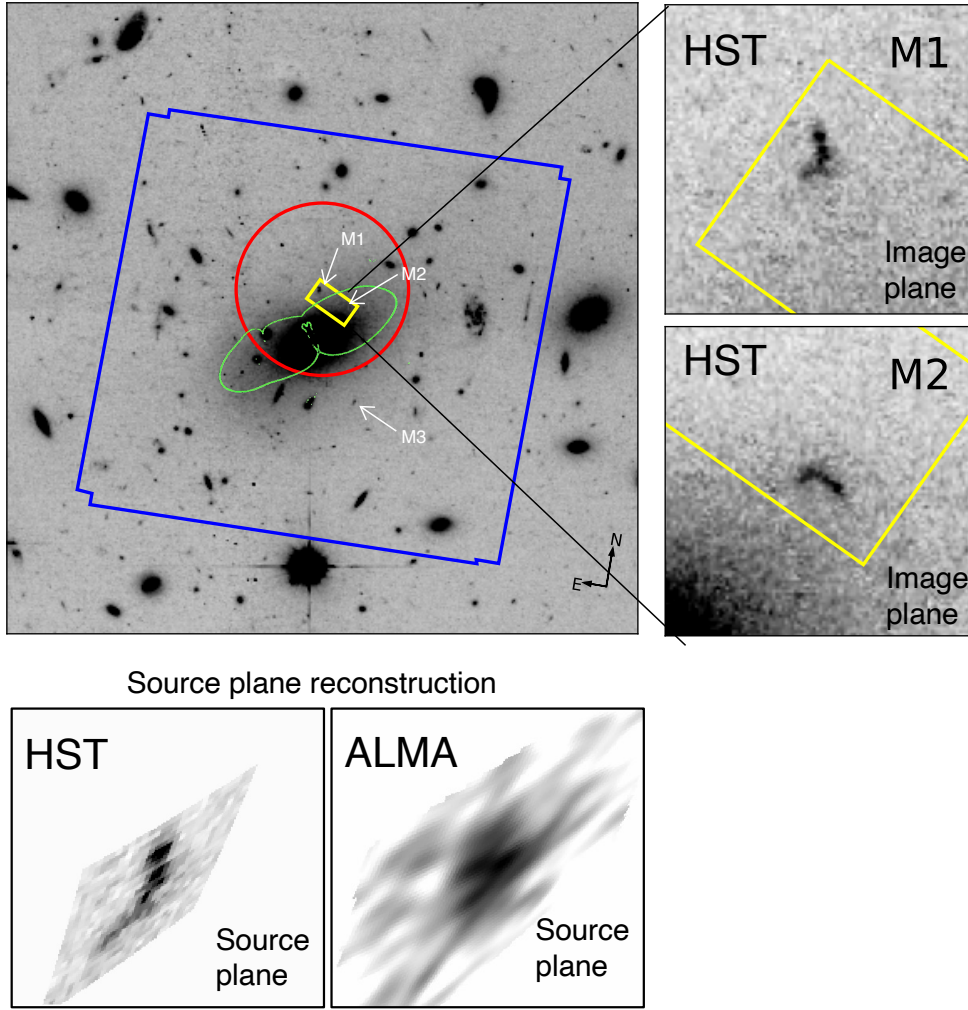
Fig. 1. Available observations for our target galaxy. Left top panel: HST/ACS WFC *F*606*W* observations shown as the background image, whereas the contours show the MUSE WFM+AO (blue) and SINFONI (yellow) field of view. The ALMA primary beam is also shown (red circle). The SINFONI and ALMA observations cover only two of the three multiple images, namely M1 and M2. The green contours show the critical lines. Right panels: M1 (top) and M2 (bottom) multiple images of our target galaxy as detected in HST data (Livermore et al. 2015; Iani et al. 2021). Both cutouts have a size of about 5″ × 5″. Bottom panels: source plane reconstruction of our target. We show both the UV continuum from HST data (left) and the [C II] emission from ALMA data (right). Both cutouts have a size of 1″ × 1″.

by the [C II] emission line (Sect. 3.3). We do not detect the continuum (see Fig. 3), which is consistent with the blue $\beta = -2.53 \pm 0.15$ slope of the galaxy as estimated from the rest-frame UV spectrum (Iani et al. 2021). In Table 2, we report the total flux density upper limit that we estimated as the 5σ uncertainty obtained when fitting, in the *uv* plane, the Fourier Transform of a 2D Gaussian model with center and FWHM fixed at the position of the [C II] detection. We also report the 5σ upper limit obtained when fitting it with the Fourier Transform of a PSF model at the location of the clumps (see Sect. 3.3).

3.3. [C II] emission line map

To find the [C II] emission line, determine the optimal channel range encompassing the emission, and create the velocity-integrated [C II] emission map of our galaxy, we ran an iterative procedure, as the one described in several literature works (e.g., Daddi et al. 2015; Zanella et al. 2018, 2023; Coogan et al. 2018). We briefly summarize it in the following. We modeled our target's emission in the *uv* plane with the GILDAS task uv_fit, adopting a two-dimensional (2D) Gaussian profile in all four

sidebands and channel per channel. To begin with, we fixed the spatial position to that determined from the optical HST images (Sect. 2.1). Using the best-fit 2D Gaussian model we extracted the one-dimensional (1D) spectrum and we searched for a positive emission line signal in the resulting spectrum. We averaged the data over the channels, maximizing the detection signal-to-noise ratio (S/N) and we fit the resulting 2D (channel-averaged) map to obtain a new best-fitting line spatial position. If this was different from the spatial position of the previous extraction, we proceeded to a new spectral extraction at the new position, and iterated the procedure until convergence was reached.

We securely detected the [C II] emission line of the most magnified image of our target, M1, at ~10σ significance (Fig. 3, Table 2). We estimated the redshift from the [C II] line in two ways, both giving consistent results (obtaining a discrepancy $\Delta z < 0.00013$): by computing the signal-weighted average frequency within the line channels and by fitting the 1D spectrum with a Gaussian function. In the following, we adopt the redshift obtained from the 1D Gaussian fit ($z_{[C II]} = 3.39548 \pm 0.00007$). We compared this redshift estimate with that obtained from the VLT/SINFONI spectrum ($z_{opt} = 3.39535 \pm 0.00025$,
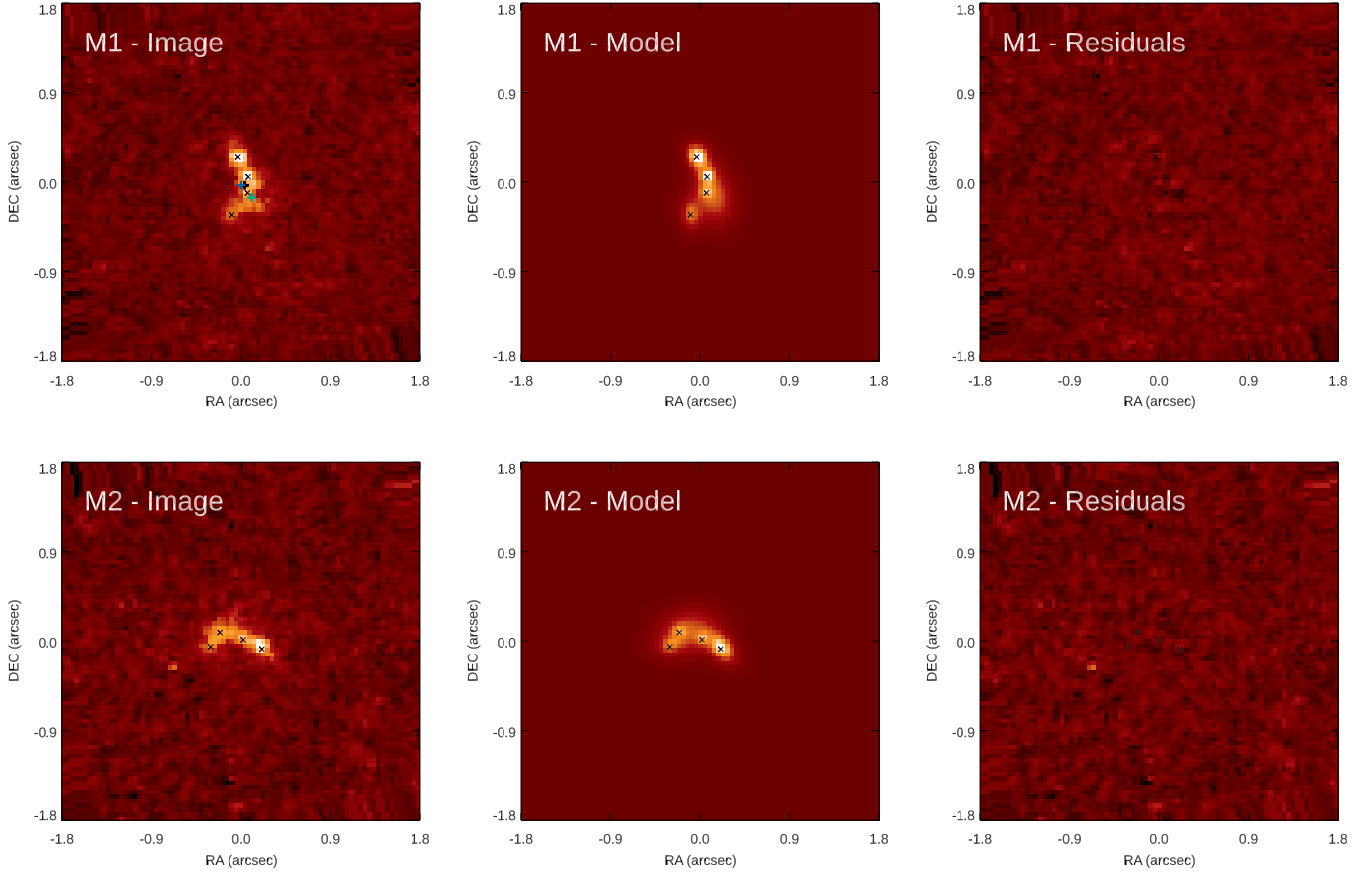
Fig. 2. GALFIT best-fit model of the UV continuum. We show the input image first column), the model (second column), and the residuals (third column) obtained by subtracting the model from the input image. Both galaxy images M1 (top row) and M2 (bottom row) are shown. The cutouts have a size of $3.6'' \times 3.6''$. The color cuts are the same in all panels of M1 and in all panels of M2. The crosses in the top left panel indicate the barycenter of the M1 galaxy image as estimated with three different methods: from the GALFIT disk-only best fit (black cross), from the GALFIT disk+clumps best fit (cyan cross), and from the SExtractor (blue cross, see Sect. 3.1 for details). The x indicate the clumps detected in the UV continuum.

Table 2. Observed far-IR properties of our target galaxy and clumps.

ID	RA (deg)	Dec (deg)	$z_{[\mathrm{C\,II}]}$	$\mu F_{[\mathrm{C\,II}]}$ (mJy)	Δv (km s^{-1})	μF_{cont} (μJy)	μF_{UV} (10^{-31} erg s^{-1} cm^{-2} Hz^{-1})	μ
(1)	(2)	(3)	(4)	(5)	(6)	(7)	(8)	(9)
Galaxy-integrated	01:18:11.184	−26:58:03.826	3.39548 ± 0.00007	7.5 ± 0.7	122	<585.9	63.3 ± 3.2	5.4 ± 0.3
Clump NE	01:18:11.196	−26:58:03.674	–	2.4 ± 0.6	61	<190.0	13.2 ± 1.2	5.1 ± 0.1
Clump SW	01:18:11.169	−26:58:03.952	–	2.5 ± 0.6	81	<190.0	<2.1	5.8 ± 0.2
Clump C (tentative)	01:18:11.175	−26:58:03.712	–	2.4 ± 0.6	41	<190.0	<2.1	5.3 ± 0.1
Clump UV-C1	01:18:11.1882	−26:58:03.866	–	–	–	–	6.6 ± 0.6	5.4 ± 0.1
Clump UV-C2	01:18:11.1892	−26:58:04.045	–	–	–	–	3.1 ± 0.3	5.7 ± 0.1
Clump UV-SE	01:18:11.2028	−26:58:04.290	–	–	–	–	10.6 ± 1.0	5.9 ± 0.1

Notes. Columns: (1) Component: galaxy-integrated and individual clump measurements are reported. All the reported measurements refer to M1. While clumps NE, SW, and C are detected in [C II], clumps UV-C1, UV-C2, and UV-SE are only detected in the UV. (2) Right ascension; (3) Declination; (4) Redshift estimated by fitting the [C II] emission line with a Gaussian in our 1D ALMA spectra. The uncertainty that we report is the formal error obtained from the fit; (5) Observed [C II] emission line flux (i.e., not corrected for lensing amplification); (6) Velocity width of the line estimated considering the channels that maximize the S/N of the detection (see Sect. 3.3); (7) 5σ upper limits on the continuum emission flux (not corrected for lensing amplification). The upper limit associated to the galaxy-integrated measurement has been obtained by considering a Gaussian model with the same structural parameters used to estimate the integrated [C II] flux (Sect. 3.3). The upper limit associated to the clump measurements has instead been obtained by considering a point-spread function (PSF) model, for consistency with the [C II] flux estimates; (8) Observed UV continuum flux density. Upper limits are 5σ; (9) Average magnification (Livermore et al. 2015; Iani et al. 2021). The coordinates of the [C II] clumps are estimated as the centroid position of 2D fit performed in the uv plane with GILDAS (Sect. 3.3). We note that, when fitting relatively low S/N sources, GILDAS centroid positions might be affected by offsets, as reported by Tan et al. (2024). However, the symmetry of the M1 and M2 images due to lensing makes the comparison of the relative position of the [C II] and UV clumps robust (see Sect. 3.7.2).
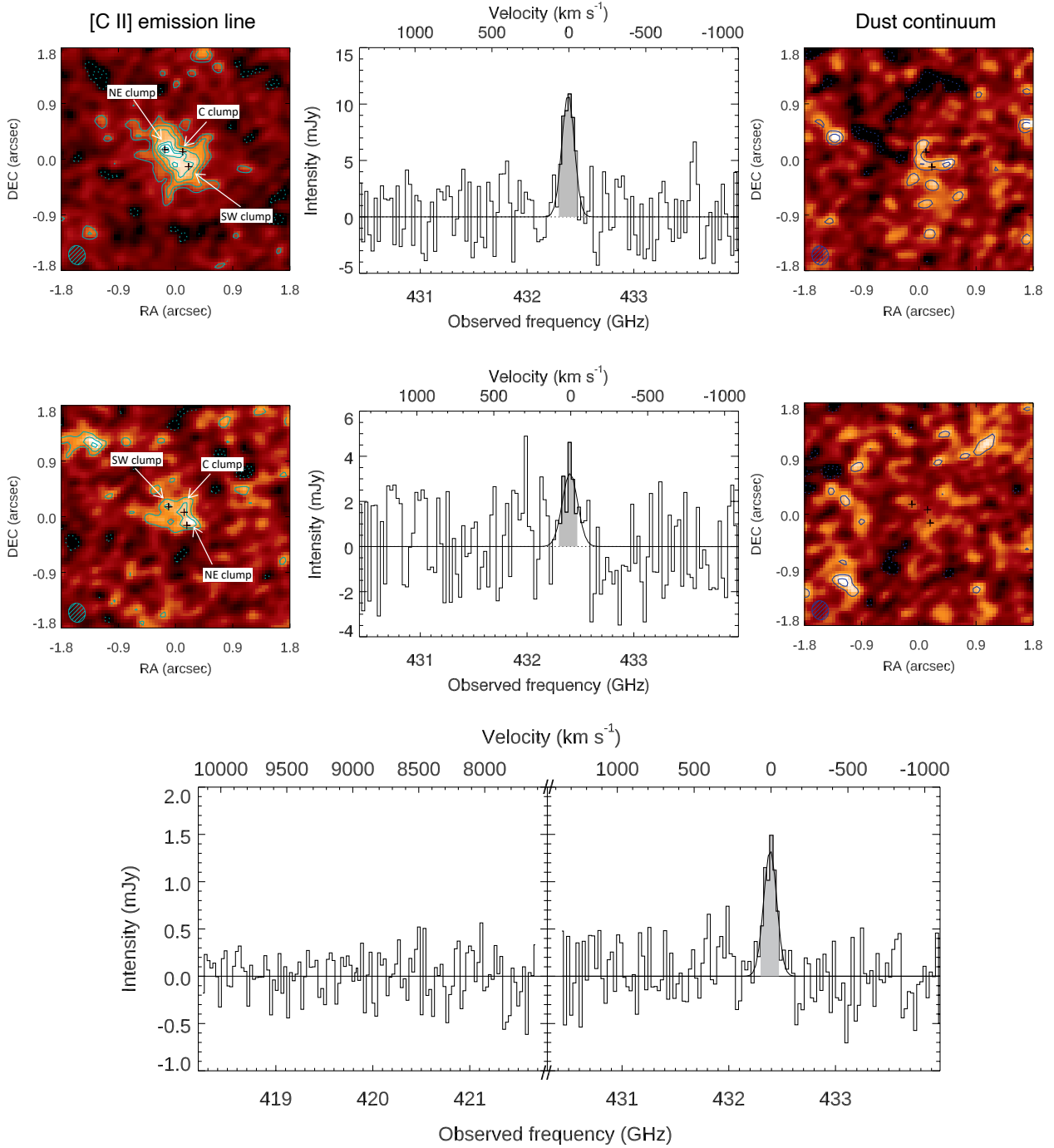
Fig. 3. ALMA data of our galaxy. Top and middle rows: images covered by the primary beam, M1 (top row) and M2 (middle row). Left panels: ALMA 2D maps of the [C II] line. The cyan solid and dashed contours indicate respectively positive and negative levels of 2, 3, 4, 5, 5.5, 6 rms. The crosses indicate the location of the [C II] clumps (NE, C, and SW as labeled on the figure). The beam is reported as the cyan ellipse. Each stamp has a size of $3.6'' \times 3.6''$. Middle panels: 1D spectrum from the ALMA datacube, extracted using the 2D Gaussian model that maximizes the S/N (Sect. 3.3). The gray shaded areas indicate the velocity range over which we measured the [C II] line flux. For illustrative purposes we also report the Gaussian fit of the emissions: it was not used to estimate the line fluxes, but only as an alternative estimate of the redshift of the galaxies (Sect. 3.3). The intensity is observed, not corrected for magnification. Right panels: ALMA 2D map of the continuum emission on the observed frequency range of 418–434 GHz. The dark blue solid and dashed contours indicate respectively positive and negative levels from 2σ to 4σ, in steps of 1σ. The intensity is observed, not corrected for magnification. Bottom row: intrinsic (magnification-corrected) stacked 1D spectrum of M1 and M2.

Iani et al. 2021) and found that they agree within 1σ, increasing the reliability of the detection.

The [C II] emission of M2, the second image of our target, is also detected, although with lower S/N due to its distance from the center of the primary beam ($\sim 5''$) and, secondary, due to its lower

magnification. We created 2D intensity maps of the [C II] emission of M2 by averaging over the same channels that maximize the detection S/N of M1 (Fig. 3). We checked that by running instead our blind, iterative procedure to determine the channels that maximize the S/N of the [C II] detection for M2 produces consistent

results: the redshift of the emission changes by $\Delta z < 0.00005$ and the width of the line changes by $\Delta FWHM < 15\,\mathrm{km\,s^{-1}}$. The [C II] emission of M2 is detected with $\sim 6\sigma$ significance. To obtain a higher S/N spectrum, we stacked the 1D spectra of M1 and M2, extracted at the best-fitting position of the Fourier Transform of the 2D Gaussian model adopted for each galaxy image. The result is shown in Fig. 3.

We finally estimated the total [C II] flux by fitting the channel-averaged emission line map of M1 in the uv plane adopting the Fourier Transform of a 2D Gaussian model with the GILDAS task uv_fit. Since the continuum was not detected, we did not subtract it. The best-fit model yields a [C II] $FWHM \sim 0.8'' \times 0.6''$, with an uncertainty of $\sim 0.1''$ on both axes. The total observed flux is $F_{\mathrm{[C II]}} = 7.5 \pm 0.7$ mJy (over $\Delta v = 122\,\mathrm{km\,s^{-1}}$). This is the total [C II] flux estimate (and best-fit model) that we use throughout the paper[2].

When subtracting the best-fit model from the data and imaging the residuals (with natural weighting), we could detect some residual emission at the location of the NE clump. Despite the low significance of the detection ($\sim 3\sigma$), its overlap with the UV brightest clump suggests the possible presence of an additional unresolved component.

The relatively low significance of clumps in the channel-averaged map is likely due to the fact that they have a narrow [C II] line (and likely a relatively small mass) implying a small contrast against a more diffuse and broader [C II] emission (if present) and/or source confusion due to crowding. Indeed, when looking at the dynamics of our target, the emission from individual clumps peaks at slightly different velocity and is rather narrow ($\sim 40-80\,\mathrm{km\,s^{-1}}$, Sect. 4.3). To assess if clumps are more prominent in narrower velocity ranges and more accurately determine their flux and significance, we searched for emission peaks in individual channel maps (Sect. 3.5). We limit the morphological decomposition of the [C II] emission to M1, due to the too low S/N of M2 that prevents a robust structural analysis.

3.4. Qualitative comparison of the [C II] and UV morphology

Studying the morphology of clumpy galaxies using different tracers (e.g., rest-frame UV continuum, optical emission lines, IR emission lines and continuum) is key to unveiling the origin and nature of clumps. We aim to understand whether the [C II] emission of our target is clumpy and if there are [C II] clumps co-spatial with those detected at UV wavelengths.

To properly compare multiwavelength datasets we accurately calibrated the absolute astrometry of the HST image. We selected 14 non-saturated and high S/N stars and compared their HST sky-coordinates with the *Gaia* DR2 catalog (Gaia Collaboration 2016, 2018). We matched the HST astrometry to *Gaia* by applying the median offsets ΔRA = 0.6600 ±

0.0300 and ΔDec = 0.0600 ± 0.0500. The absolute astrometry of the ALMA data, instead, is very accurate and there is no need to further refine it (Farren et al. 2021).
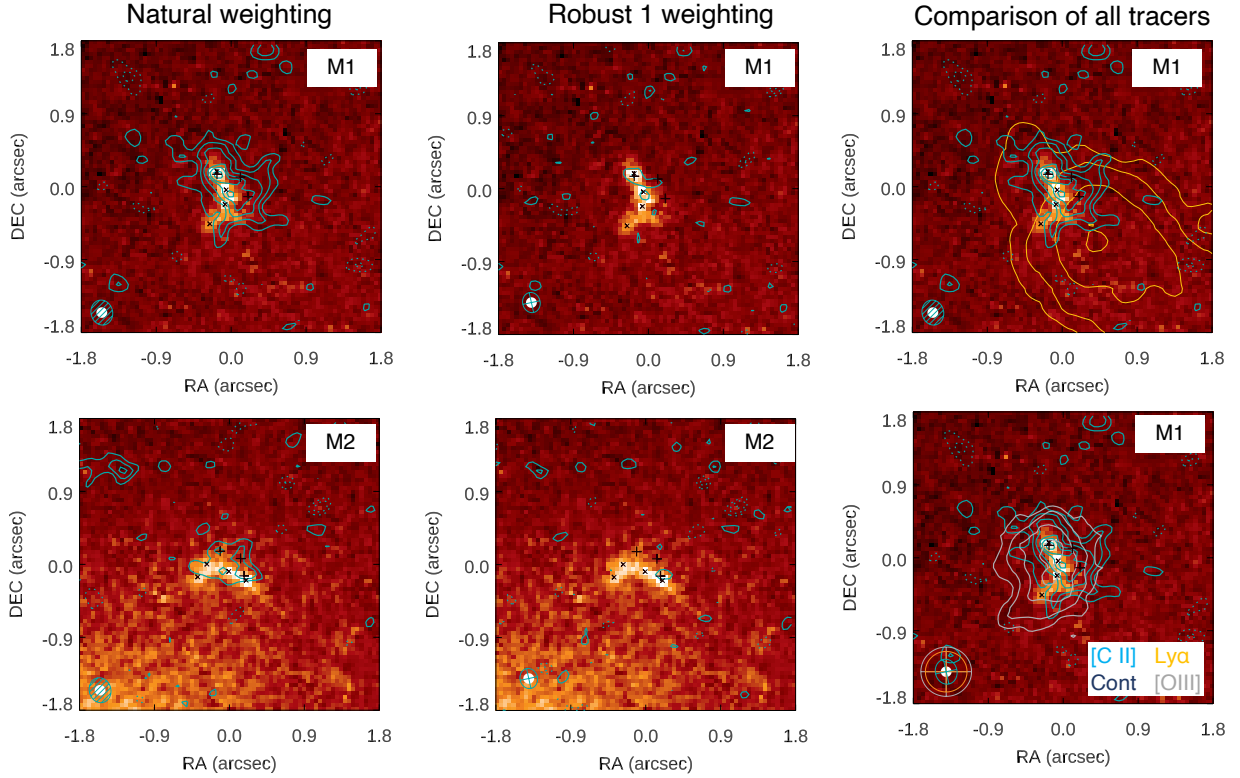
In Fig. 4, we compare the morphology of the UV continuum with that of the channel-averaged 2D [C II] map obtained as described in Sect. 3.3. The peak of the [C II] coincides with the brightest clump detected in the HST image (in the following we refer to this clump as "NE clump", as it is located in the northeastern side of the galaxy). The [C II] also shows a diffuse component largely overlapping with the UV continuum, despite being ~ 1.8 times more extended (see Sect. 3.3). In particular, the [C II] extends to a region where no UV is detected. A channel-by-channel analysis reveals the presence of a clump in that area (Sects. 3.5 and 4.3). In the following, we refer to this [C II]-bright and UV-dark component as "SW clump" because it is located in the southwestern side of the galaxy. In between the NE clump and the SW one there is one more compact emission that is visible in the 2D [C II] map and in the channel-by-channel analysis. It results in a tentative ($>2.5\sigma$) detection over two consecutive channels (Sect. 3.5). In the following, we label this clump as "central (C) clump". We report it in the analysis below for completeness, although further observations are needed to confirm its detection.

Despite the lower S/N, also in M2 the [C II] peak coincides with the brightest UV clump and the [C II] emission extends to a region where the UV is not detected, as in the case of M1. This similarity and the symmetry of the [C II] morphology of M1 and M2, which is expected given that the critical line passes in between these two galaxy images (Sect. 2.2), gives credit to the fact that the NE and SW clumps are actual star-forming regions rather than noise peaks (see also a more detailed discussion on this in Sect. 3.7).

With the aim of increasing the spatial resolution of the observations, we also imaged the ALMA data using the "robust" (instead of "natural") weighting from GILDAS, with parameter 1, yielding a beam size of $FWHM = 0.23'' \times 0.19''$ and a noise rms of 0.23 mJy beam^{-1}, over a bandwidth of $102\,\mathrm{km\,s^{-1}}$, corresponding to the velocity width encompassed by the [C II] emission (Sect. 2.3). As expected, the diffuse [C II] component is barely detected as it is resolved out, while the peak of the emission is still compact and detected in both M1 and M2. The C clump is tentatively detected in the 2D map of M1.

To assess whether the different morphology of the UV continuum and the [C II] emission could arise from instrumental differences between optical and interferometric observations and/or observational biases, we used the CASA tasks SIMOBSERVE and SIMANALYSE to create mock ALMA [C II] maps. We considered the best-fit parametric model obtained by fitting the UV image (Sect. 3.1) and created mock [C II] maps with the same angular resolution and rms as our actual ALMA observations. Figure A.1 shows the mock maps of M1 imaged by using both natural and robust (with parameter 1) weighting. The morphology of the emission is clearly different from that of the actual [C II] morphology: the peak of the emission coincides with the barycenter of the UV continuum and, when fitting it with a 2D elliptical Gaussian in the uv plane, we recover sizes of $FWHM \sim 0.4'' \times 0.2''$, while the actual [C II] emission has sizes of $FWHM \sim 0.8'' \times 0.6''$ (Sect. 3.3). The NE clump is visible in the mock [C II] maps, especially when robust weighting is used for the imaging. This suggests that the different morphology of [C II] and UV emission are due to physical reasons rather than instrumental issues.

In Fig. 4 we show the morphology of the other available tracers, namely the Hβ, [O III], and Lyα emission lines. While the

---

[2] We also checked whether a channel-by-channel fit would yield consistent results. In particular, we fit each channel encompassing the [C II] emission with the Fourier Transform of a 2D Gaussian, with the center coordinates and the FWHM free to vary during the fit. We obtain a total observed [C II] flux $F_{\mathrm{[C II]}} = 10.5 \pm 1.2$ mJy over $\Delta v = 122\,\mathrm{km\,s^{-1}}$, consistent within 2σ with the previous estimate. This method allows for the recentering of the model in case the center and size of the emission changes with the frequency (or velocity). However, it might have the drawback of including positive noise peaks in the accounting of the flux. As a further check, we also fit the emission channel-by-channel with position and size of the model fixed to the values obtained by fitting the high S/N, channel-averaged map. In this case we estimate a flux $F_{\mathrm{[C II]}} = 8.4 \pm 0.7$ mJy, consistent within $\sim 1\sigma$ with both the other estimates.

Natural weighting

Robust 1 weighting

Comparison of all tracers

Fig. 4. Comparison of UV and [C II] morphology of our galaxy. We show both images covered by the primary beam, M1 and M2 (as indicated in the labels). Left panels: HST UV continuum data (background image) overlaid with the [C II] data obtained with natural weighting (contours). The cyan solid and dashed contours indicate respectively positive and negative levels of 2, 3, 4, 5, 5.5, 6 rms. The crosses indicate the location of the clumps detected in [C II], while the x indicate the location of the clumps detected in UV continuum. The ALMA beam is reported as the cyan ellipse, while the HST PSF is reported as the white-filled ellipse. Middle panels: HST UV continuum data (background image) overlaid with the [C II] data obtained with GILDAS using robust weighting and a parameter of 1 (contours). Contour levels are the same as in the left panels. Right panels: comparison of the available tracers for the galaxy image M1: UV continuum (background), [C II] (cyan contours as in previous stamps), Lyα (orange contours with levels of 3, 5, 10, 18 rms, in the top panel), [O III] (gray contours with levels of 3, 5, 8, 11 rms in the bottom panel). The beams of each tracer are reported in the bottom right panel. All stamps have a size of $3.6'' \times 3.6''$.

optical lines (Hβ and [O III]) are spatially coincident with the UV emission, the Lyα instead is spatially offset by ~0.16″ ± 0.02″ that, at the redshift of our target, corresponds to 1.2 ± 0.2 kpc (de-lensed). A detailed analysis and comparison of the UV, Hβ, [O III], and Lyα morphologies has already been presented by Iani et al. (2021). For the present study we mainly focus on the morphology of the UV continuum from HST and the [C II] emission from ALMA.

3.5. Identifying clumps in the [C II] channel maps

To identify clumps in individual channel maps, we followed an approach similar to the one developed by Dessauges-Zavadsky et al. (2019, 2023) to find GMCs in CO(4−3) observations of two lensed, $z \sim 1$ galaxies. We imaged individual channel maps using natural weighting and identified all the ≥4σ emissions within a radius corresponding to 1/3 of the primary beam. We then searched for all the spatially overlapping >3σ emissions with the pre-identified emissions in at least two adjacent $20.3 \, \mathrm{km \, s^{-1}}$ channel maps. This allows us to exclude spurious noise peaks that are instead expected to be randomly distributed. Indeed, all the detections satisfying the above criteria are found to be co-spatial with the integrated [C II] emission of M1. We considered as individual clumps those with 3σ contours that are not spatially overlapping with each other in the same channel map or, if co-spatial, they are separated by at least one chan-

nel (i.e., they are not adjacent). In other words, different clumps could overlap spatially or in velocity, but not both. We identified three such clumps: the NE clump (spatially coincident with the brightest UV clump) is detected in 3 adjacent channels; the SW clump (not detected in the UV) is detected in 4 adjacent channels; finally clump C is detected in only 2 adjacent channels. We consider clump C as "tentative" as it was detected in only two channels. More observations with higher S/N are needed to confirm it.

3.6. Measuring clumps [C II] flux

We measured the flux of clumps both in the image plane and in the uv plane and compared the results. To measure fluxes in the image plane, we adopted customized apertures in each channel, such that they encompass all the emission above the local rms noise level. With this approach no aperture correction is needed. For each clump, the line-integrated fluxes were obtained by summing up the flux estimated in each adjacent channel (Dessauges-Zavadsky et al. 2023).

We also estimated the flux of each clump by fitting its emission in the uv plane. When adopting Gaussian models, we obtain consistent results with those estimated from the image plane both in terms of flux and size (Table C.1). The FWHM of the best-fit Gaussians range between 0.26″ and 0.60″, corresponding to $800-1.9$ pc after magnification correction, in agreement

with the FWHM radii we estimated from the 2D Gaussian fits performed in the channel maps encompassing the brightest [C II] emission of each identified clump. The sizes of the best-fit Gaussians are 3 to 8 times larger than the sizes measured for the UV clumps of our target (Sect. 3.1). They are also larger than typical GMC sizes measured using CO in lensed galaxies at $z \sim 1$ (Dessauges-Zavadsky et al. 2019, 2023). We might be detecting kpc-scale [C II] substructures, possibly due to the blending of smaller structures that are unresolved at the resolution of our observations. Alternatively, there might be some diffuse, intra-clump [C II] emission where clumps are embedded, similarly to what is commonly seen in optical emission line maps (e.g., Förster Schreiber et al. 2011; Zanella et al. 2015, 2019). To investigate the second scenario, we also fit the clumps identified in channel maps with the Fourier Transform of 2D PSF models, representing compact clumps (radius <400 pc) embedded in a more diffuse and broader emission. The center coordinates of the PSF models were left free during the fit (i.e., we did not fix them to the position of expected clumps). We obtain flux estimates for the SW, NE, and C clumps that are 1.2−1.5 times smaller than the Gaussian fit case (Table C.1). The discussion of whether to subtract possible intra-clump light or not when estimating the flux of clumps is a longstanding and unsolved issue at any wavelength (e.g., Förster Schreiber et al. 2011; Wuyts et al. 2012) and goes beyond the scope of this work. Recent theoretical works suggest that most of the [C II] is emitted in dense photodissociation regions associated with molecular clouds rather than in the diffuse, neutral medium due to the relatively high critical density of [C II] ($\sim$3000 cc) which is not achievable in the diffuse medium (Pallottini et al. 2017b; Vallini et al. 2017; Olsen et al. 2017). We decided to adopt the flux measurements obtained by fitting clumps with PSF models (Table 2), as they are expect to be unresolved at the resolution of our observations (e.g., the size of the giant molecular clouds found in lensed galaxies at $z \sim 1$ is $R < 200$ pc, Dessauges-Zavadsky et al. 2023). We report the other flux estimates in Table C.1. Even when adopting fluxes obtained with the other reported methods, the conclusions of our work do not change substantially. All fluxes have been corrected for lensing effects by considering the average magnification at the location of each clump.

3.7. Reliability of clump [C II] detection

We performed additional tests to assess if the detected compact, spatially unresolved [C II] components are physical entities (i.e., molecular clouds) or just peaks of correlated noise. In particular, we performed the following tests: we assessed whether point sources are needed to reproduce the radial amplitude of the [C II] data; we computed the probability that the clumps are noise peaks given the symmetry of M1 and M2 offered by lensing; and we created mock [C II] observations to understand what are the features that we expect to detect in actual [C II] maps. We detail such tests in the following.

3.7.1. Radial amplitude analysis

We extract the amplitude of the signal as a function of the uv-distance, namely the baseline length, for the spectral channels spanning the [C II] emission. For a point source, the amplitude is constant as a function of the uv distance, while for an extended source the amplitude is maximum at short uv distances and decreases at larger uv distances. If the source is extended, we can determine its size and flux by fitting a 1D half-Gaussian profile to the radial amplitude profile. The physical size of the
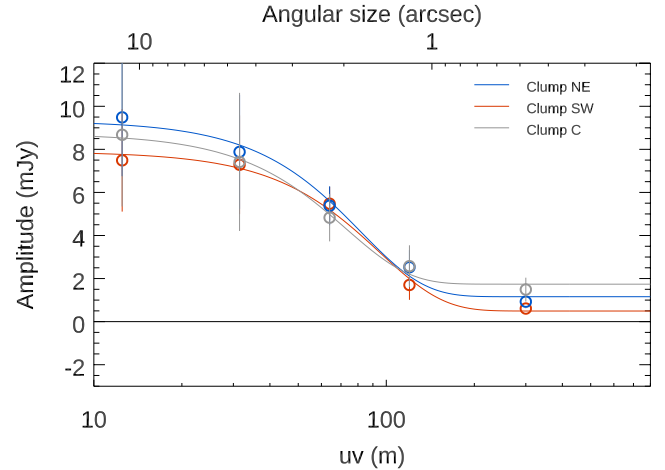
Fig. 5. Signal amplitude as a function of the uv distance, namely the baseline length. We extracted the signal amplitude at three different spatial locations, coinciding with the NE clump (blue), the SW clump (red), and the C clump (gray). We fit each dataset with a Gaussian model plus a constant. In the image plane these best-fit functions correspond to a Gaussian with $FWHM \sim 2''$ and a PSF component. An additional constant, corresponding to another PSF component, is needed to fit the measurements.

source is related to the FWHM of the Gaussian, while its total flux is the peak value of the Gaussian. Figure 5 shows the radial amplitude of the [C II] as a function of the uv distance for M1, at the spatial position of the NE, SW, and C clumps.

A Gaussian model with $FWHM \sim 2''$ is needed to fit the data at short baselines, implying that the source is resolved. Its flux ranges between $F_{[C II],Gauss} \sim 8-10$ mJy/μ, depending on the extraction position, consistent with that estimated from the parametric modeling of the 2D surface brightness of the emission (Sect. 3.3). We note that these are all observed estimates (i.e., not corrected for magnification). However, an additional PSF (i.e., spatially unresolved) component is also needed to fit the longest baselines (i.e., shortest angular size) of the datasets extracted at the position of the clumps. This is shown by the fact that the amplitude of the signal remains constant at the longest uv distances and does not go to zero. This supports the presence of unresolved [C II] components in addition to the more extended emission.

3.7.2. Probability of the [C II] clumps being noise peaks

Our target is a lensed galaxy and two images, M1 and M2, are inside the primary beam. For both images, the peak of the [C II] emission coincides with the NE clump. In this Section, we assess whether the detected clump is an actual physical component of the galaxy or if it is an artifact, such as a noise peak, on top of an extended emission. To this aim, we calculated the probability of having a $>3.5\sigma$ noise peak at a distance ranging between $0.35''$ and $0.45''$ from the barycenter, mimicking the compact [C II] clump that is detected in our dataset. In the primary beam, we injected at random positions a 2D Gaussian model with the same structural parameters obtained from the 2D fit of the [C II] emission (Sect. 3.3). With the CASA tasks `simobserve` and `simanalyze` we simulated 1000 mock [C II] maps and in each of them used SExtractor to automatically detect noise peaks on top of the extended (Gaussian) emission. We then fit the detected peaks in the uv plane with a point-like model. We computed the probability of finding noise peaks that have a $>3.5\sigma$

Table 3. Physical properties of our target galaxy and clumps.

| ID | M_{mol} | SFR | Σ_{mol} | Σ_{SFR} | t_{dep} | R_{UV} | $R_{[C II]}$ |
| | $(10^8\ M_\odot)$ | $(M_\odot\ \mathrm{yr}^{-1})$ | $(M_\odot\ \mathrm{pc}^{-1})$ | $(M_\odot\ \mathrm{yr}^{-1}\ \mathrm{kpc}^{-2})$ | (Gyr) | (pc) | (pc) |
(1)	(2)	(3)	(4)	(5)	(6)	(7)	(8)
Galaxy-integrated	20.5 ± 2.0	10.1 ± 0.5	734.5 ± 59.9	2.4 ± 0.2	0.38 ± 0.04	736	1352×950
Clump NE	3.5 ± 0.9	2.2 ± 0.2	1158.1 ± 281.7	7.3 ± 0.1	0.16 ± 0.04	251	$<311\ ^{(\star)}$
Clump SW	4.3 ± 1.0	<0.3	852.8 ± 200.7	<0.6	>1.35	–	<399
Clump C (tentative)	2.2 ± 0.5	<0.3	408.5 ± 100.0	<0.6	>0.65	–	<418
Clump UV-C1	–	1.1 ± 0.1	–	–	–	<207	–
Clump UV-C2	–	0.5 ± 0.04	–	–	–	<202	–
Clump UV-SE	–	1.6 ± 0.1	–	–	–	391	–

Notes. All properties have been corrected for magnification. Columns: (1) Galaxy ID; (2) Molecular gas mass obtained from the [C II] luminosity; (3) Star formation rate obtained from the UV luminosity; (4) Molecular gas surface density. For the [C II]-detected clumps this is computed by considering the $R_{[C II]}$ upper limit as the size of the clump; (5) SFR surface density for the [C II]-detected clumps. The $R_{[C II]}$ upper limit is considered as the size of the clump, for consistency with the Σ_{mol} estimate. If we were to consider the R_{UV} instead our conclusions would not change substantially; (6) Depletion time; (7) Effective radius of the UV continuum emission; (8) Semi-major and semi-minor axis of the [C II] line emission, when resolved, and semi-minor axis upper limit (corresponding to the beam semi-minor axis) when unresolved. All properties listed here are intrinsic (i.e., corrected for magnification). $^{(\star)}$This clump is detected also when using "robust" weighting with parameter 1 (instead of "natural" which is instead used to detect the other clumps). We determine the upper limit on the size of the NE clump from the semi-minor axis of the beam obtained with robust weighting, while for the SW and C clump we consider the beam size obtained with "natural" weighting.

significance and a distance from the Gaussian center in the range $0.35'' - 0.45''$, consistent with the actual distance of our [C II] clump from the galaxy barycenter (distance ~$0.4''$). We estimate a probability of 19% of finding such a noise peak. However, our [C II] is detected both in M1 and M2 and, in both cases, it coincides with the NE clump or, in other words, it has a specific position which is symmetric with respect to the critical line. We calculated the probability of having two noise peaks detected at >3.5σ, within $0.35'' - 0.45''$ from the galaxy barycenter, and with a symmetric position (e.g., being in the N–E side of the galaxy) to be 0.08%. This shows that the compact [C II] component overlapped with the NE clump is very likely to be a physical structure and not simply an observational artifact due to correlated noise or other instrumental effects. Analogous calculations hold also for the other [C II] clumps which are tentatively detected both in M1 and M2 as elongations of the [C II] emission in regions where no UV flux is detected (Fig. 3). The extremely low probability (<1%) of having a symmetric noise peak with respect to the critical line makes the detection of these [C II] clumps reliable.

4. Results

In the following, we discuss the physical properties of our target galaxy and clumps as derived from the observables presented in previous sections.

4.1. Star formation rate

We estimated the star formation rate from the luminosity of the rest-frame UV continuum at 1500 Å. In particular, we considered the HST imaging and modeled the 2D surface brightness profile of our target with GALFIT (Sect. 3.1) to obtain the UV luminosity of individual clumps, as well as the total integrated one. We applied the recipes by Kennicutt (1998), after reporting them to a Chabrier (2003) IMF, and obtained an estimate of the SFR. The galaxy has a total, unobscured, magnification-corrected star formation rate SFR ~ $10 \pm 0.3\ M_\odot\ \mathrm{yr}^{-1}$ (Table 3). The clumps have unobscured SFR ~ $0.5 - 2\ M_\odot\ \mathrm{yr}^{-1}$ each, accounting in total for ~5%–20% of the UV light from the galaxy, as generally found

both in lensed and non-lensed high-redshift star-forming regions (e.g., Guo et al. 2018; Zanella et al. 2019; Meštrić et al. 2022; Claeyssens et al. 2023).

Our total, integrated SFR estimate is in agreement with that reported by Iani et al. (2021), who estimated it from the luminosity of the Hβ emission line extracted from the SINFONI 1D spectrum. They used the Hβ-to-SFR conversion factor by Kennicutt (1998), reported to a Chabrier (2003) IMF, and obtained SFR(Hβ) = $9.9 \pm 2.3\ M_\odot\ \mathrm{yr}^{-1}$. We did not correct the UV and Hβ luminosity for dust extinction as the reddening that we estimated from the UV continuum β slope is consistent with no dust extinction (Iani et al. 2021). This is also in agreement with the lack of dust continuum detection (Sects. 3.2 and 5.2). In Table 3 we also report the SFR and SFR surface density (Σ_{SFR}) of individual clumps.

4.2. Molecular gas mass

We estimated the molecular gas mass of our target from the [C II] luminosity. We considered a [C II] luminosity-to-gas mass conversion factor $\alpha_{[C II]} = 31\ M_\odot/L_\odot$ (with a scatter of 0.3 dex) as estimated by Zanella et al. (2018). A comparable $\alpha_{[C II]}$ conversion factor has been estimated and used to derive molecular gas masses by other literature studies for galaxies at similar redshift (Dessauges-Zavadsky et al. 2020; Gururajan et al. 2023; Béthermin et al. 2023) and in the local Universe (Madden et al. 2020; Ramambason et al. 2024), and it has been validated by theoretical arguments and simulations (Pallottini et al. 2017a; Sommovigo et al. 2021; Vizgan et al. 2022).

We obtain a total molecular gas mass for our galaxy, corrected for magnification, $M_{H2} = (2.05 \pm 0.20) \times 10^9\ M_\odot$ (Table 3). This uncertainty accounts only for the errors related to the [C II] luminosity. If we were to take into account also the uncertainties related to the $\alpha_{[C II]}$ conversion factor and magnification correction, the errors associated to M_{H2} would be ~0.33 dex larger. Such uncertainties do not account for systematic differences in the (unconstrained) H I content of high-redshift galaxies. In fact, since [C II] has a lower ionization potential than H I (11.3 eV for [C II] versus 13.6 eV for H I), part of the [C II] emission could arise from any gas phase (molecular, ionized, and atomic). However, it has been shown that the majority of the [C II]

luminosity ($\gtrsim 60-95\%$) is emitted by photodissociation regions (PDRs) and hence is associated with molecular gas, especially in the inner galaxy regions (e.g., Stacey et al. 1991; Sargsyan et al. 2012; Pineda et al. 2013; Velusamy & Langer 2014; Rigopoulou et al. 2014; Cormier et al. 2015; Croxall et al. 2017; Diaz-Santos et al. 2017). This is supported also by simulations showing that $\sim 60-85\%$ of the [C II] is emitted by the molecular gas phase (e.g., Vallini et al. 2015; Olsen et al. 2017; Accurso et al. 2017, although see Heintz et al. 2021 for a discussion of [C II] as an H I tracer). Given that the H I fraction is unconstrained at the redshift of our source and that we are studying the inner kpc of the galaxy, where the H_2 is expected to dominate over the H I, we assume that the molecular gas is the main contributor to the [C II] emission (Combes 2001). In Table 3 we report the M_{H2} and molecular gas mass surface density (Σ_{mol}) of individual clumps.

4.3. Dynamical properties

We investigated the dynamics of our target by looking at the position-velocity (PV) diagram. PV diagrams are slices extracted from the data cube, along specific spatial directions. Figure 6 shows the PV diagram of the [C II] emission extracted along the axis connecting the two detected [C II] clumps. Distinct components are detected, separated by $\sim 0.3''$ and $\sim 50\,\mathrm{km\,s^{-1}}$. The component with negative velocity and spatial offset is mostly due to the NE clump, while the other more elongated emission is likely due to the contribution of several components (clump SW and clump C). To assess whether this is indeed the case, we created an emission map averaging the channels that are red-shifted with respect to the systemic [C II] redshift and a second map averaging the blue-shifted channels (Fig. 6). The first map (red-shifted channels) shows mainly the SW clump (positive offset with respect to the galaxy barycenter) plus a "bridge" emission connecting it with the NE clump location. The second map (blue-shifted channels) instead shows the NE clump and the region around the galaxy barycenter. These findings are in agreement with the results obtained by analyzing individual channel maps (Sect. 3.5) and support the result that the [C II] emission is made of multiple, distinct components.

Finally, we created moment maps with the `immoments` task of the CASA software. We adopted a 2.5σ threshold above the rms noise level. The moment-0 (intensity), moment-1 (velocity), and moment-2 (velocity dispersion) maps are shown in Fig. 6. They are not corrected for beam-smearing, instrumental line spread function, nor lensing effects. In the moment-0 map the SW clump appears more clearly than in the intensity map, likely due to its relatively large velocity dispersion (see also the moment-2 map), while the NE clump is not prominent in the moment-0 map due to its narrow velocity width. The moment-1 map does not show ordered rotation. The velocity dispersion ranges between 10 and $35\,\mathrm{km\,s^{-1}}$, it peaks on the SW clump and reaches its minimum in the external regions of the galaxy, which are also less affected by beam smearing. This seems to be a dispersion-dominated galaxy and similar results are found when considering the moment maps reconstructed in the source plane (Fig. B.1). The galaxy appears dispersion-dominated also when the [O III] 5007 Å line emission is considered, as reported by Livermore et al. (2015, although the [O III] observations are seeing-limited and hence have coarser angular resolution than the [C II] data used in our study). The dispersion-dominated nature of the galaxy disfavors the formation of the observed clumps due to violent disk instability in an isolated, rotationally supported disk (e.g., Dekel & Burkert 2014; Bournaud et al.

2014; Ceverino et al. 2015; Tamburello et al. 2015). The kinematics of the galaxy rather suggests that these clumps formed as a consequence of a recent interaction, although we do not detect companion galaxies within the primary beam (up to $\sim 100\,\mathrm{kpc}$ distance from our target). Alternatively, one of the clumps might be an ex situ object, such as a low-mass galaxy, merging with our target and giving rise to both its dispersion-dominated dynamics and the formation of clumps due to gas instability and fragmentation (Teyssier et al. 2010; Bournaud et al. 2011; Renaud et al. 2014; Calabrò et al. 2019; Zanella et al. 2019). In the following, the contribution of rotation to the observed velocity dispersion is neglected. However, more robust dynamical modeling, which is beyond the scope of this paper, is needed to confirm and refine these findings.

4.4. Expected size of clumps from gravitational instability

We investigated whether we should indeed expect to detect clumps given the resolution of our observations, the gas mass surface density of our target galaxy, and its velocity dispersion. Molecular clouds that form in situ due to the gas gravitational instability, are expected to have an average size that is comparable to the Jeans length:

$$\lambda_J = \frac{\sigma^2}{2\pi G \Sigma_{gas}} \tag{1}$$

where G is the gravitational constant, Σ_{gas} is the gas surface density, and σ is the gas velocity dispersion within the disk (Toomre 1964; Elmegreen et al. 2009; Elmegreen 2009; Cañameras et al. 2017; Gullberg et al. 2018). We estimated the magnification-corrected gas surface density of the galaxy $\Sigma_{gas} = 525\,M_\odot\,\mathrm{pc}^{-2}$ by considering its molecular gas mass as estimated from the [C II] luminosity (Sect. 4.2) and the size of the extended [C II] emission (Sect. 3.3). From the moment-2 map (Fig. 6) we measure velocity dispersions in the range $\sigma \sim 10-35\,\mathrm{km\,s^{-1}}$, where the smallest velocity dispersion is found in the outskirts of the galaxy which is less affected by beam smearing. The integrated velocity dispersion of the [C II] line is $\sigma \sim 37\,\mathrm{km\,s^{-1}}$ and once we correct it for the instrumental broadening we obtain an intrinsic velocity dispersion $\sigma_{int} \sim 20\,\mathrm{km\,s^{-1}}$. By adopting an average velocity dispersion $\sigma \sim 20\,\mathrm{km\,s^{-1}}$, we obtain gravitationally unstable scales $\lambda_J \sim 100\,\mathrm{pc}$ which are compatible with the fact that our [C II] clumps are unresolved (i.e., appear as point-like sources) at the resolution of our observations (beam $FWHM = 0.26'' \times 0.31''$ that corresponds to $R_e \lesssim 400\,\mathrm{pc}$ after correcting for lensing magnification). Turbulence and gravitational collapse are expected to trigger the generation of stars inside these parent molecular clouds (Elmegreen 2009). The clumps are characterized by high density ($\Sigma_{gas} > 10^3\,M_\odot\,\mathrm{pc}^{-2}$) and high gravitational pressure, $P_{grav}/k_b \sim G\Sigma_{gas}^2 > 10^7\,\mathrm{K\,cm^{-3}}$. Such extreme pressure values are typical of the most highly pressurized medium in molecular clouds of star-forming galaxies (Elmegreen & Efremov 1997; Calura et al. 2022). This scenario is broadly consistent with the fact that we detect clumps in the UV continuum images, with effective radii $R_e \lesssim 250\,\mathrm{pc}$ (Table 3).

5. Discussion

5.1. Gas depletion time and Schmidt–Kennicutt plane

By comparing the SFR and molecular gas mass surface densities of galaxies and clumps in the traditional Schmidt–Kennicutt (SK) plane (Schmidt 1959; Kennicutt 1998), it is possible to assess their depletion time $t_{dep} \sim \Sigma_{mol}/\Sigma_{SFR} \sim M_{H2}/\mathrm{SFR}$. This
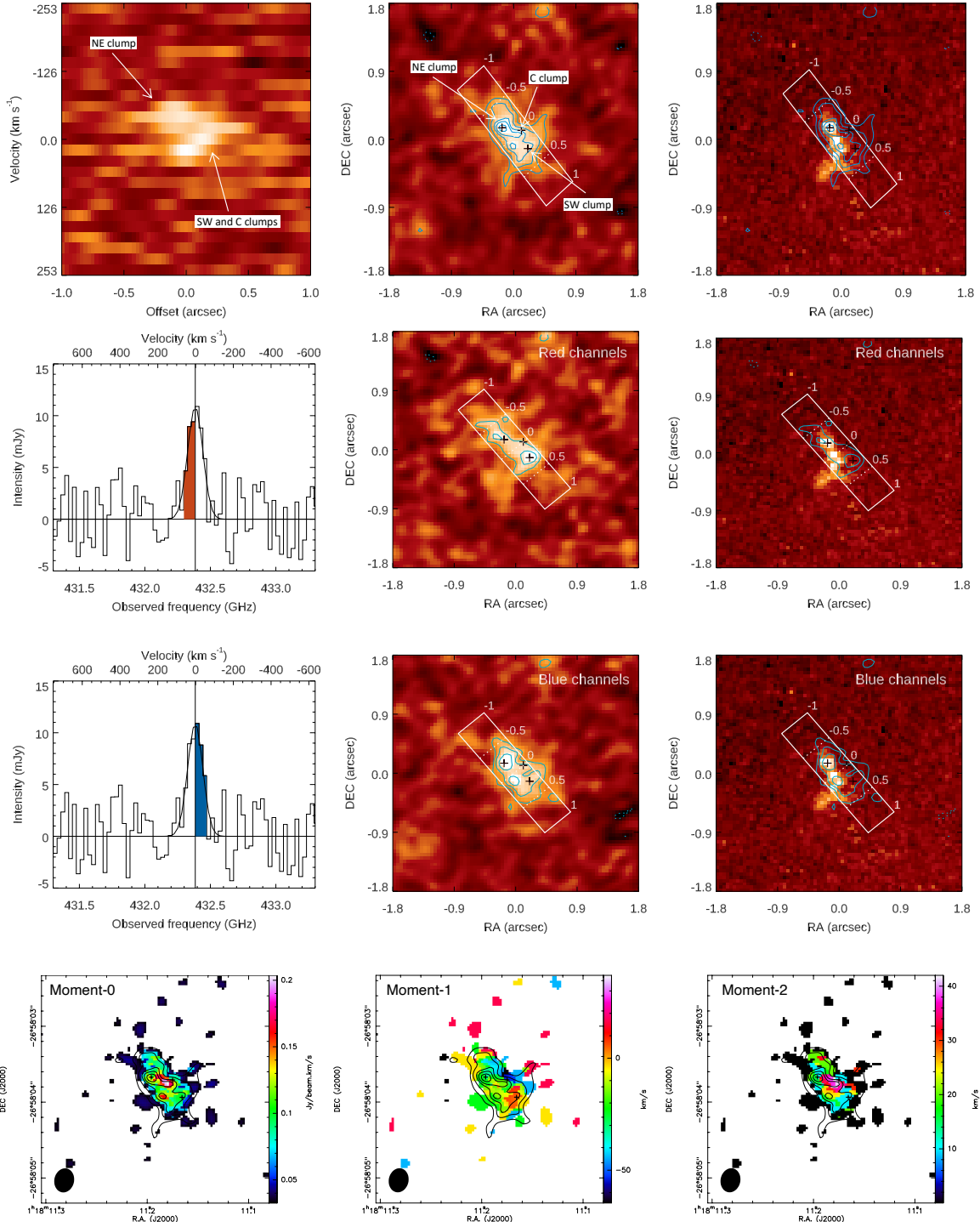
Fig. 6. Dynamical properties of M1. First row, left panel: position-velocity diagram of the [C II] emission extracted along the slit shown in the next panels. First row, middle panel: [C II] map (background) overlaid with the [C II] (3, 4, 5, 5.5, 6) rms contours (cyan) and the slit used to extract the PV diagram (white). The dashed lines mark offsets of 0.5″ along the slit. First row, right panel: UV continuum imaging (background) and [C II] contours overlaid. Second row, left panel: 1D spectrum showing the integrated [C II] emission. In red we highlight the channels used to create the intensity map shown in the next panel. Second row, middle panel: [C II] intensity map obtained by averaging only the channels with positive velocity with respect to systemic ("red channels") overlaid with (3, 4, 5) rms contours. Second row, right panel: UV continuum (background), with [C II] contours. Other symbols are as in previous panels. Third row, left panel: 1D [C II] spectrum, with channels used to produce the intensity maps of the next panel highlighted in blue. Third row, middle panel: [C II] intensity map obtained by averaging only the channels with negative velocity with respect to systemic ("blue channels") with [C II] (3, 4, 5) rms contours (cyan) overlaid. Other symbols are as in previous panels. Third row, right panel: UV continuum (background) with [C II] contours overlaid. Symbols are as in previous panels. Fourth row, left panel: moment-0 map. Fourth row, middle panel: moment-1 map. Fourth row, right panel: moment-2 map. The contours are estimated from the intensity map and are the same as in Fig. 6. The black ellipse in the bottom left corner indicates the beam size. The crosses indicate the location of [C II] clumps.
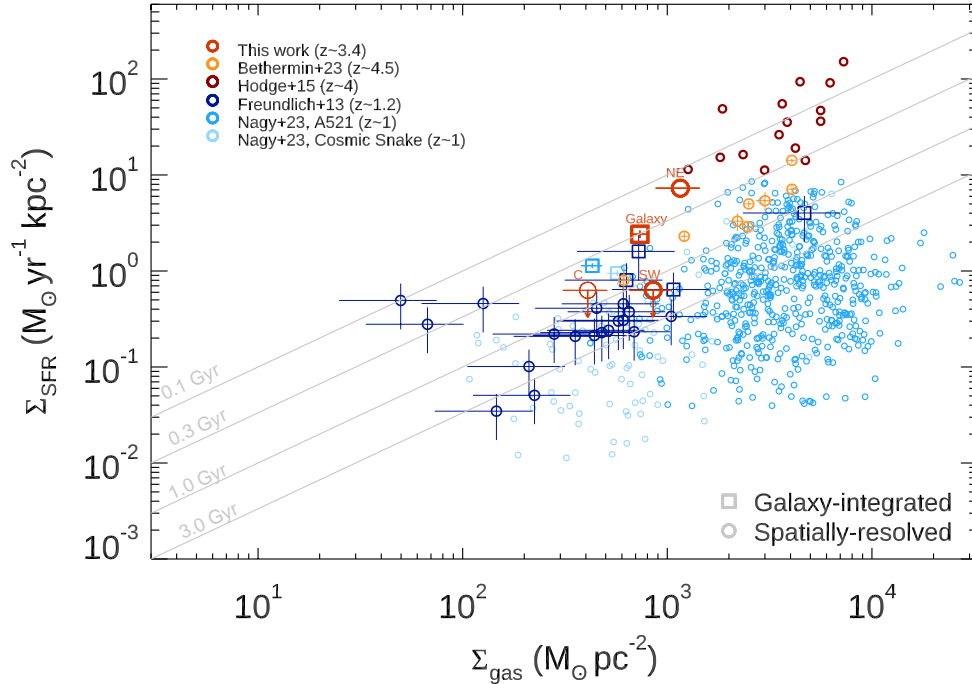
Fig. 7. Clumps location in the Schmidt–Kennicutt plane. We compare our findings (red symbols), with available subkiloparsec observations from the literature at $z \sim 1-4$ (colored symbols, Freundlich et al. 2013; Hodge et al. 2015; Nagy et al. 2023; Béthermin et al. 2023). Galaxy-integrated measurements are reported as squares, while spatially resolved measurements as circles. Clump C, which is considered as tentative, is indicated with the red, thinner, circle. We also indicate lines of constant depletion time (gray lines).

ratio indicates the time that is needed to turn the molecular gas reservoir into stars, assuming a constant SFR. The molecular gas and young stars are expected to be co-spatial at the scale of individual GMCs if the star formation happens in quasi-equilibrium for several dynamical times. On the contrary, if the star formation process happens quickly and GMCs are disrupted soon after the formation of the first massive stars, then molecular gas and young stars are decorrelated at the small scales (Schruba et al. 2010; Kruijssen et al. 2019; Kim et al. 2022; Nagy et al. 2023). Spatially resolved studies are crucial to constrain what is the depletion time at subkiloparsec scales and unveil the possible (de)correlation between star-forming regions and GMCs. Figure 7 shows the location of our galaxy and clumps in the $\Sigma_{mol}-\Sigma_{SFR}$ plane, and compares it with literature galaxies and their subkiloparsec regions (Freundlich et al. 2013; Hodge et al. 2015; Nagy et al. 2023; Béthermin et al. 2023). We only included galaxies at $z \sim 1-4$ and their subkiloparsec regions that are detected at sub-mm wavelengths. In Fig. 7 we show the SFR and M_{mol} surface densities averaged over an area of $\sim 400\,pc$ radius, which is the physical scale corresponding to the angular resolution of the observations. This is consistent with the area considered to estimate surface densities of sub-galactic regions in the literature (Freundlich et al. 2013; Hodge et al. 2015; Nagy et al. 2023; Béthermin et al. 2023). Adopting smaller sizes would not change our results (e.g., depletion time estimates), as the location of clumps in the SK plane would change along the curves of iso-depletion time. Our [C II]-detected clumps span a large range of depletion time. The NE clump, which is detected both in UV and [C II], has a very short $t_{dep} = 0.16 \pm 0.04\,Gyr$. On the contrary, the SW and C clumps, which are not detected in the UV, have a rather long $t_{dep} > 0.65\,Gyr$. We compare our results with the depletion time of individual sub-galactic regions in apertures of $\sim 400\,pc$

in radius from two $z \sim 1$, strongly lensed galaxies: the Cosmic Snake and A521 (Nagy et al. 2023)[3]. The apertures of $\sim 400\,pc$ in radius (in the source plane) are comparable to the size upper limit of our clumps (Table 3). The depletion time in such regions is on average $t_{dep} > 1\,Gyr$, although a large scatter is observed (Fig. 7). One of the reasons reported by Nagy et al. (2023) to explain the scatter of the SK at subkiloparsec scales is the fact that the t_{dep} measurements largely depend on whether they are performed in apertures dominated by star-forming regions (i.e., UV peaks) or GMCs (i.e., CO peaks). Randomly selected regions might have a large range of t_{dep}, depending on whether they capture only one phase (star-forming vs gaseous) or both. The average depletion time observed in the Cosmic Snake and A521 is in good agreement with the t_{dep} upper limits estimated for our SW and C clumps. The fact that no UV continuum is observed at the location of the [C II] emission of these regions, implying a rather long gas depletion timescale, might indicate that we are witnessing the onset of star formation, when the molecular gas reservoir has not been consumed or disrupted yet and the star formation is still embedded. The fact that no SFR is detected in these regions might also be due to the fact that the UV continuum is tracing stellar populations with ages $\sim 100\,Myr$, which might not be present yet. Observations of tracers probing earlier phases of star formation (e.g., Hα emission probing ages $\lesssim 10\,Myr$) are needed to assess whether young stellar populations are present in these regions. On the contrary, the NE clump has a $\sim 4\times$ shorter depletion time than the average t_{dep} of subkiloparsec regions in the Cosmic Snake and A521, rather comparable to sub-galactic regions found in starbursts (Hodge et al. 2015) and $z \sim 4$ galaxies (Béthermin et al. 2023). Other spatially resolved studies of high-redshift galaxies (Rawle et al. 2014; Chen et al. 2017;

---

[3] We rescaled the SFR from Nagy et al. (2023) to a Chabrier (2003) IMF, to properly compare with the SFR estimated for our clumps.

Calura et al. 2021) showed regions with short depletion time $t_{\text{dep}} \sim 100$ Myr, although we do not include them in Fig. 7 as they encompass larger sizes ($\gtrsim 1$ kpc) than our observations and/or have higher redshift ($z \gtrsim 5$). One possible explanation for the short depletion time of the NE clump is the fact that an intense and rather long-lasting episode of star formation is ongoing in this region, possibly implying molecular gas replenishment from the surrounding regions to sustain star formation over ~100 Myr timescale (the time span probed by the UV continuum). Another possibility is the fact that the UV and [C II] emission are spatially decorrelated over scales <300−400 pc, which are not resolved with our observations, and therefore they appear co-spatial because of the lack of angular resolution. Observations with resolution ~0.05″−0.1″ (corresponding to $\lesssim 150$ pc in the source plane) are needed to shed light on this.

5.2. The lack of dust continuum

Besides the [C II] line emission, our ALMA observations also probe the dust continuum at wavelength $\lambda_{\text{obs}} \sim 700\,\mu$m (corresponding to rest-frame $\lambda_{\text{rf}} \sim 160\,\mu$m). The continuum is not detected in the 1D spectrum nor in the 2D maps (Sect. 3.2)[4]. We estimated a 5σ continuum upper limit for M1 by fitting a Gaussian model or a PSF model in the uv plane (see Sect. 3.2). We corrected both upper limits for lensing effects, by applying an average magnification correction. We obtain a continuum flux 5σ upper limit of $F_{\text{cont}} < 105\,\mu$Jy when considering a Gaussian model and $F_{\text{cont}} < 34\,\mu$Jy when considering a PSF model. These are more stringent upper limits than most values reported in the literature for galaxies at similar redshift. Koprowski et al. (2020) targeted the 870 μm dust continuum for a sample of 250 Lyman Break Galaxies (LBGs) at $z \sim 3$ and obtained 41 detections. By stacking the non-detections, they obtained a tentative 3.2σ detection with a total flux of $F_{870\,\mu\text{Jy}} = 65 \pm 20\,\mu$Jy. Similar results are obtained by Coppin et al. (2015) that, by stacking the 850 μm continuum data of LBGs at $z \sim 3$ and $z \sim 4$ obtained average fluxes $F_{850\,\mu\text{Jy}} = 250 \pm 30\,\mu$Jy at $z \sim 3$ and $F_{850\,\mu\text{Jy}} = 410 \pm 30\,\mu$Jy at $z \sim 4$. The 850 μm dust content of main-sequence $z \sim 4.5−6$ galaxies was also investigated by the ALPINE survey (Béthermin et al. 2020): 23 target galaxies out of 118 were detected with $F_{850\,\mu\text{Jy}} \gtrsim 115\,\mu$Jy. Non detections were stacked in bins of [C II] luminosity and yielded average continuum fluxes $\langle F_{850\,\mu\text{m}} \rangle \sim 50−300\,\mu$Jy (Béthermin et al. 2020), approaching the upper limit of our target. Finally, Capak et al. (2015) analyzed individual LBGs at $z \sim 5$ and estimated from their non-detections a 3σ upper limit $F_{850\,\mu\text{m}} \lesssim 30\,\mu$Jy, comparable to ours. Hence, lensing magnification allowed us to place an upper limit on the continuum flux which is more stringent than most of those estimated for (non-lensed) galaxies at similar redshift. Our result is consistent with the blue slope of the UV continuum $\beta = -2.53 \pm 0.15$ and the reddening $E(B-V)_{\text{cont}} < 0.16$ mag estimated from the optical data (Iani et al. 2021), indicating that star formation is mostly unobscured in our target.

However the question remains about the SW clump that we detected in [C II], but not at UV or IR continuum wavelengths. We estimated the total IR luminosity (L_{IR}) of the SW clump by multiplying the 158 μm continuum upper limit of the SW clump by the ratio between the monochromatic continuum luminosity (νL_ν) and the L_{IR} at the rest-frame wavelength associated with the [C II] line emission ($\nu L_\nu / L_{\text{IR}} = 0.133$), as reported by Bethermin et al. (2017), Béthermin et al. (2020) for galaxies at similar redshift. We obtain an upper limit on the total IR luminosity $L_{\text{IR}} < 5 \times 10^8\,L_\odot$. Finally, by adopting the L_{IR}-to-SFR conversion proposed by Kennicutt (1998), converted to a Chabrier (2003) IMF, we placed an upper limit on the obscured SFR of the SW clump SFR $\lesssim 0.1\,M_\odot$ yr^{-1}. This is consistent with the 3σ unobscured SFR upper limit that we obtained from the UV from the SW clump (SFR $< 0.3\,M_\odot$ yr^{-1}) and with the typical SFR of clumps at these redshifts which is in the range SFR $\sim 0.01−10\,M_\odot$ yr^{-1} (e.g., Guo et al. 2018; Zanella et al. 2019; Meštrić et al. 2022; Claeyssens et al. 2023). Finally, from the [C II] luminosity of the SW clump into SFR, adopting the relation by De Looze et al. (2014) for starbursts, we obtain SFR$_{[\text{C II}]} = 0.3 \pm 0.1$. If we were to adopt the SFR-to-[C II] conversion factor estimated for high-redshift galaxies instead (De Looze et al. 2014), we would obtain similar results (SFR$_{[\text{C II}]} = 0.2 \pm 0.1$), consistent with the estimate derived from the UV and with the non-detection in the ALMA continuum map. This suggests that greater sensitivity (hence deeper observations and/or larger magnification) is needed to detect the IR continuum emission of individual clumps.

It has been suggested that the clumps ubiquitously detected at UV and optical wavelengths could be an effect of dust inhomogeneities across the galaxy disk that make the UV light appear patchy, enhancing some small dust-free structures while hiding the most attenuated ones (Buck et al. 2017). While attenuation could indeed play an important role in dusty submillimeter galaxies (Hodge et al. 2016; Rujopakarn et al. 2016; Ivison et al. 2020), in lower mass, dust-poor galaxies such as our target, the physical properties of individual clumps seem to be mostly unaffected by dust. The fact that the NE clump of our target is also detected in [C II] which, unlike the UV, is not strongly affected by dust, supports the scenario in which clumps in low-mass galaxies are actual physical structures. Finally, the non-detection of the far-IR continuum emission implies that the offset between the Lyα and UV continuum emission (Sect. 2.1 and Fig. 4) in this galaxy is likely caused by scattering due to the presence of neutral gas rather than dust.

6. Summary and conclusions

We investigated the [C II] emission of a clumpy galaxy at redshift $z \sim 3.4$ lensed by the foreground galaxy cluster Abell 2895. Our ALMA data cover two multiple images of the target, M1 and M2. Additional ancillary data from HST (probing the rest-frame UV continuum), VLT/MUSE (probing the Lyα emission), and VLT/SINFONI (probing the [O III] and Hβ emissions) are available. We found that:

- The spatially integrated [C II] emission is detected at ~10σ significance. It mostly overlaps with the rest-frame UV continuum emission from HST, but it is ~1.8 times spatially more extended.
- We detected the [C II] emission of individual clumps that we labeled NE, SW, and C. The NE clump coincides with the brightest clump detected in the UV continuum, while the SW and C clumps are not detected in the available HST imaging. Both images, M1 and M2, show comparable morphology, although M2 is observed with lower S/N due to the fact that it is located ~5″ away from the center of the ALMA

---

primary beam (and secondary it also has slightly lower magnification).

– Our observations do not resolve the [C II] clumps, yielding intrinsic (magnification-corrected) radii $R_e \lesssim 300-400$ pc. The fact that they are not resolved is in agreement with expectations for molecular clouds formed by fragmentation due to gravitational instabilities, yielding Jeans unstable scales $\lambda_J \sim 100$ pc, given the velocity dispersion and the molecular gas surface density of our target.

– The galaxy is dispersion-dominated as shown by the position-velocity diagram and moment maps. This indicates that the formation of clumps likely did not occur due to gravitational disk instability in an isolated disk, but it is rather induced by a merger. We did not detect any galaxy interacting with our target within ~ 100 kpc, although one of the clumps might actually have an ex situ origin and be the remnant of the merging satellite.

– We estimated the molecular gas mass of individual clumps from their [C II] luminosity, adopting the conversion factor proposed by Zanella et al. (2018, but see also Dessauges-Zavadsky et al. 2020; Madden et al. 2020). We find $M_{mol} \sim 10^8\,M_\odot$. The NE clump, which is detected both in [C II] and UV, has a short depletion time $t_{dep} = 0.16 \pm 0.04$ Gyr, comparable with sub-galactic regions in high-redshift galaxies (Hodge et al. 2015; Béthermin et al. 2023). The SW and C clumps instead have longer depletion time ($t_{dep} > 0.65$ Gyr), similar to $z \sim 1$ sub-galactic regions (Freundlich et al. 2013; Nagy et al. 2023).

– We do not detect the dust continuum down to $F_{cont} < 34\,\mu$Jy. This is consistent with the blue UV continuum slope ($\beta \sim -2.53 \pm 0.15$) estimated from the VLT/MUSE data (Iani et al. 2021). The continuum non-detection is consistent with the SFR upper limit derived from the UV (SFR$_{UV} < 0.3\,M_\odot\,\text{yr}^{-1}$) and from the [C II] when adopting the De Looze et al. (2014) conversion (SFR$_{[C II]} < 0.3\,M_\odot\,\text{yr}^{-1}$). Deeper observations are needed to detect the dust continuum of individual clumps. This also suggests that in low-mass galaxies such as our target, clump detection is not significantly affected by dust distribution and inhomogeneities (Buck et al. 2017).

Exquisite spatial resolution and sensitivity are needed to detect clumps and their parent molecular clouds. Most high-redshift studies aiming to detect the dust continuum, CO, or [C II] emission of individual clumps yielded tentative or non-detections (Cibinel et al. 2015; Gullberg et al. 2015; Hodge et al. 2016; Rujopakarn et al. 2019; Ivison et al. 2020; Calura et al. 2021). This might be due to a number of reasons: the relatively coarse spatial resolution of the observations and/or lack of sensitivity (e.g., Cibinel et al. 2015; Calura et al. 2021), the short depletion time of molecular clouds, and/or the fact that the targets were submillimeter galaxies that are bright in the IR, but not observed at UV wavelengths, hence it is unknown whether they host UV clumps in the first place (Gullberg et al. 2018; Hodge et al. 2016; Rujopakarn et al. 2019; Ivison et al. 2020). Gravitational lensing allowed Dessauges-Zavadsky et al. (2019, 2023) to achieve greater sensitivity and spatial resolution and detect the CO(4−3) emission from individual molecular clouds hosted by two main-sequence, clumpy galaxies at $z \sim 1$. Our work extends the detection of clumps at sub-mm wavelengths up to $z \sim 3.4$ and suggests that [C II] is a promising tracer of molecular clouds at high redshift. Larger samples of lensed clumps observed with [C II] will be needed to further strengthen our conclusions. The simultaneous availability of other tracers (e.g., dust-continuum and/or CO emission) will allow us to constrain further the physical proper-

ties of molecular clouds down to scales of hundreds of pc and pinpoint the initial conditions for clumps formation.

References

Accurso, G., Saintonge, A., Bisbas, T. G., & Viti, S. 2017, MNRAS, 464, 3315
Bertin, E., & Arnouts, S. 1996, A&AS, 117, 393
Bethermin, M., Wu, H.-Y., Lagache, G., et al. 2017, A&A, 607, A89
Béthermin, M., Fudamoto, Y., Ginolfi, M., et al. 2020, A&A, 643, A2
Béthermin, M., Accard, C., Guillaume, C., et al. 2023, A&A, 680, L8
Bolamperti, A., Zanella, A., Mestric, U., et al. 2023, MNRAS, 526, 5263
Bolatto, A. D., Wolfire, M., & Leroy, A. K. 2013, ARA&A, 51, 207
Bournaud, F., Dekel, A., Teyssier, R., et al. 2011, ApJ, 741, L33
Bournaud, F., Perret, V., Renaud, F., et al. 2014, ApJ, 780, 57
Bournaud, F., Daddi, E., Weiß, A., et al. 2015, A&A, 575, A56
Buck, T., Macciò, A. V., Obreja, A., et al. 2017, MNRAS, 468, 3628
Calabrò, A., Daddi, E., Fensch, J., et al. 2019, A&A, 632, A98
Calura, F., Vanzella, E., Carniani, S., et al. 2021, MNRAS, 500, 3083
Calura, F., Lupi, A., Rosdahl, J., et al. 2022, MNRAS, 516, 5914
Cañameras, R., Nesvadba, N., Kneissl, R., et al. 2017, A&A, 604, A117
Capak, P. L., Carilli, C., Jones, G., et al. 2015, Nature, 522, 455
Carilli, C. L., & Walter, F. 2013, ARA&A, 51, 105
Cava, A., Schaerer, D., Richard, J., et al. 2018, Nat. Astron., 2, 76
Ceverino, D., Dekel, A., Tweed, D., & Primack, J. 2015, MNRAS, 447, 3291
Chabrier, G. 2003, PASP, 115, 763
Chen, C.-C., Hodge, J. A., Smail, I., et al. 2017, ApJ, 846, 108
Chevance, M., Kruijssen, J. M. D., Hygate, A. P. S., et al. 2020, MNRAS, 493, 2872
Cibinel, A., Le Floc'h, E., Perret, V., et al. 2015, ApJ, 805, 181
Claeyssens, A., Adamo, A., Richard, J., et al. 2023, MNRAS, 520, 2180
Combes, F. 2001, Astrophys. Space Sci. Suppl., 277, 29
Conselice, C. J. 2014, ARA&A, 52, 291
Conselice, C. J., Grogin, N. A., Jogee, S., et al. 2004, ApJ, 600, L139
Coogan, R. T., Daddi, E., Sargent, M. T., et al. 2018, MNRAS, 479, 703
Coppin, K. E. K., Geach, J. E., Almaini, O., et al. 2015, MNRAS, 446, 1293
Cormier, D., Madden, S. C., Lebouteiller, V., et al. 2015, A&A, 578, A53
Croxall, K. V., Smith, J. D., Pellegrini, E., et al. 2017, ApJ, 845, 96
Daddi, E., Dannerbauer, H., Liu, D., et al. 2015, A&A, 577, A46
Dekel, A., & Burkert, A. 2014, MNRAS, 438, 1870
De Looze, I., Baes, M., Zibetti, S., et al. 2010, A&A, 518, L54
De Looze, I., Cormier, D., Lebouteiller, V., et al. 2014, A&A, 568, A62
Dessauges-Zavadsky, M., Richard, J., Combes, F., et al. 2019, Nat. Astron., 3, 1115
Dessauges-Zavadsky, M., Ginolfi, M., Pozzi, F., et al. 2020, A&A, 643, A5
Dessauges-Zavadsky, M., Richard, J., Combes, F., et al. 2023, MNRAS, 519, 6222
Diaz-Santos, T., Armus, L., Charmandaris, V., et al. 2017, ApJ, 846, 32
Elíasdóttir, Á., Limousin, M., Richard, J., et al. 2007, arXiv e-prints [arXiv:0710.5636]
Elmegreen, B. G. 2009, in The Galaxy Disk in Cosmological Context, eds. J. Andersen, B. Nordström, & J. Bland-Hawthorn, 254, 289
Elmegreen, B. G., & Efremov, Y. N. 1997, ApJ, 480, 235
Elmegreen, B. G., & Elmegreen, D. M. 2005, ApJ, 627, 632
Elmegreen, B. G., Bournaud, F., & Elmegreen, D. M. 2008, ApJ, 688, 67
Elmegreen, B. G., Elmegreen, D. M., Fernandez, M. X., & Lemonias, J. J. 2009, ApJ, 692, 12
Faber, S. M., & Jackson, R. E. 1976, ApJ, 204, 668

Farren, G. S., Partridge, B., Kneissl, R., et al. 2021, ApJS, 256, 19
Ferrara, A., Vallini, L., Pallottini, A., et al. 2019, MNRAS, 489, 1
Förster Schreiber, N. M., Shapley, A. E., Genzel, R., et al. 2011, ApJ, 739, 45
Freeman, P., Rosolowsky, E., Kruijssen, J. M. D., Bastian, N., & Adamo, A. 2017, MNRAS, 468, 1769
Freundlich, J., Combes, F., Tacconi, L. J., et al. 2013, A&A, 553, A130
Gaia Collaboration (Brown, A. G. A., et al.) 2016, A&A, 595, A2
Gaia Collaboration (Brown, A. G. A., et al.) 2018, A&A, 616, A1
Graciá-Carpio, J., Sturm, E., Hailey-Dunsheath, S., et al. 2011, ApJ, 728, L7
Guilloteau, S., & Lucas, R. 2000, in Imaging at Radio through Submillimeter Wavelengths, eds. J. G. Mangum, & S. J. E. Radford, ASP Conf. Ser., 217, 299
Gullberg, B., De Breuck, C., Vieira, J. D., et al. 2015, MNRAS, 449, 2883
Gullberg, B., Swinbank, A. M., Smail, I., et al. 2018, ApJ, 859, 12
Guo, Y., Ferguson, H. C., Bell, E. F., et al. 2015, ApJ, 800, 39
Guo, Y., Rafelski, M., Bell, E. F., et al. 2018, ApJ, 853, 108
Gururajan, G., Bethermin, M., Sulzenauer, N., et al. 2023, A&A, 676, A89
Heintz, K. E., Watson, D., Oesch, P. A., Narayanan, D., & Madden, S. C. 2021, ApJ, 922, 147
Hodge, J. A., Riechers, D., Decarli, R., et al. 2015, ApJ, 798, L18
Hodge, J. A., Swinbank, A. M., Simpson, J. M., et al. 2016, ApJ, 833, 103
Hodge, J. A., Smail, I., Walter, F., et al. 2019, ApJ, 876, 130
Huertas-Company, M., Iyer, K. G., Angeloudi, E., et al. 2024, A&A, 685, A48
Iani, E., Zanella, A., Vernet, J., et al. 2021, MNRAS, 507, 3830
Iani, E., Zanella, A., Vernet, J., et al. 2023, MNRAS, 518, 5018
Ivison, R. J., Richard, J., Biggs, A. D., et al. 2020, MNRAS, 495, L1
Jullo, E., Kneib, J. P., Limousin, M., et al. 2007, New J. Phys., 9, 447
Kalita, B. S., Silverman, J. D., Daddi, E., et al. 2024, ApJ, 960, 25
Kennicutt, R. C., Jr. 1998, ApJ, 498, 541
Kim, J.-G., Ostriker, E. C., & Filippova, N. 2021, ApJ, 911, 128
Kim, J., Chevance, M., Kruijssen, J. M. D., et al. 2022, MNRAS, 516, 3006
Koprowski, M. P., Coppin, K. E. K., Geach, J. E., et al. 2020, MNRAS, 492, 4927
Kruijssen, J. M. D., Schruba, A., Chevance, M., et al. 2019, Nature, 569, 519
Leung, T. K. D., Pallottini, A., Ferrara, A., & Mac Low, M.-M. 2020, ApJ, 895, 24
Liu, D., Förster Schreiber, N. M., Genzel, R., et al. 2023, ApJ, 942, 98
Livermore, R. C., Jones, T. A., Richard, J., et al. 2015, MNRAS, 450, 1812
Madden, S. C., Cormier, D., Hony, S., et al. 2020, A&A, 643, A141
Mandelker, N., Dekel, A., Ceverino, D., et al. 2017, MNRAS, 464, 635
McMullin, J. P., Waters, B., Schiebel, D., Young, W., & Golap, K. 2007, in Astronomical Data Analysis Software and Systems XVI, eds. R. A. Shaw, F. Hill, & D. J. Bell, ASP Conf. Ser., 376, 127
Messa, M., Dessauges-Zavadsky, M., Richard, J., et al. 2022, MNRAS, 516, 2420
Meštrić, U., Vanzella, E., Zanella, A., et al. 2022, MNRAS, 516, 3532

Miville-Deschênes, M.-A., Murray, N., & Lee, E. J. 2017, ApJ, 834, 57
Nagy, D., Dessauges-Zavadsky, M., Messa, M., et al. 2023, A&A, 678, A183
Oke, J. B. 1974, ApJ, 189, L47
Olsen, K., Greve, T. R., Narayanan, D., et al. 2017, ApJ, 846, 105
Pallottini, A., Ferrara, A., Gallerani, S., et al. 2017a, MNRAS, 465, 2540
Pallottini, A., Ferrara, A., Bovino, S., et al. 2017b, MNRAS, 471, 4128
Peng, C. Y., Ho, L. C., Impey, C. D., & Rix, H.-W. 2002, AJ, 124, 266
Peng, Y.-J., Lilly, S. J., Kovač, K., et al. 2010, ApJ, 721, 193
Pineda, J. L., Langer, W. D., Velusamy, T., & Goldsmith, P. F. 2013, A&A, 554, A103
Ramambason, L., Lebouteiller, V., Madden, S. C., et al. 2024, A&A, 681, A14
Rawle, T. D., Egami, E., Bussmann, R. S., et al. 2014, ApJ, 783, 59
Renaud, F., Bournaud, F., Kraljic, K., & Duc, P. A. 2014, MNRAS, 442, L33
Richard, J., Smith, G. P., Kneib, J.-P., et al. 2010, MNRAS, 404, 325
Richard, J., Jauzac, M., Limousin, M., et al. 2014, MNRAS, 444, 268
Rigopoulou, D., Hopwood, R., Magdis, G. E., et al. 2014, ApJ, 781, L15
Rujopakarn, W., Dunlop, J. S., Rieke, G. H., et al. 2016, ApJ, 833, 12
Rujopakarn, W., Daddi, E., Rieke, G. H., et al. 2019, ApJ, 882, 107
Sargsyan, L., Lebouteiller, V., Weedman, D., et al. 2012, ApJ, 755, 171
Schmidt, M. 1959, ApJ, 129, 243
Schruba, A., Leroy, A. K., Walter, F., Sandstrom, K., & Rosolowsky, E. 2010, ApJ, 722, 1699
Shibuya, T., Ouchi, M., Kubo, M., & Harikane, Y. 2016, ApJ, 821, 72
Sommovigo, L., Ferrara, A., Carniani, S., et al. 2021, MNRAS, 503, 4878
Stacey, G. J., Geis, N., Genzel, R., et al. 1991, ApJ, 373, 423
Tadaki, K., Iono, D., Yun, M. S., et al. 2018, Nature, 560, 613
Tamburello, V., Mayer, L., Shen, S., & Wadsley, J. 2015, MNRAS, 453, 2490
Tan, Q. H., Daddi, E., de Souza Magalhães, V., et al. 2024, A&A, 684, A23
Teyssier, R., Chapon, D., & Bournaud, F. 2010, ApJ, 720, L149
Toomre, A. 1964, ApJ, 139, 1217
Ushio, K., Ohta, K., Maeda, F., Hatsukade, B., & Yabe, K. 2021, ApJ, 909, 84
Vallini, L., Gallerani, S., Ferrara, A., Pallottini, A., & Yue, B. 2015, ApJ, 813, 36
Vallini, L., Ferrara, A., Pallottini, A., & Gallerani, S. 2017, MNRAS, 467, 1300
Vanzella, E., Calura, F., Meneghetti, M., et al. 2017a, MNRAS, 467, 4304
Vanzella, E., Castellano, M., Meneghetti, M., et al. 2017b, ApJ, 842, 47
Vanzella, E., Caminha, G. B., Rosati, P., et al. 2021, A&A, 646, A57
Vanzella, E., Castellano, M., Bergamini, P., et al. 2022, A&A, 659, A2
Velusamy, T., & Langer, W. D. 2014, A&A, 572, A45
Vizgan, D., Greve, T. R., Olsen, K. P., et al. 2022, ApJ, 929, 92
Wuyts, S., Förster Schreiber, N. M., Genzel, R., et al. 2012, ApJ, 753, 114
Zanella, A., Daddi, E., Le Floc'h, E., et al. 2015, Nature, 521, 54
Zanella, A., Daddi, E., Magdis, G., et al. 2018, MNRAS, 481, 1976
Zanella, A., Le Floc'h, E., Harrison, C. M., et al. 2019, MNRAS, 489, 2792
Zanella, A., Pallottini, A., Ferrara, A., et al. 2021, MNRAS, 500, 118
Zanella, A., Valentino, F., Gallazzi, A., et al. 2023, MNRAS, 524, 923

Appendix A: Mock [C II] maps

To check whether the [C II] and UV light distribution is intrinsically different and not an observational effect, we created mock [C II] maps with the CASA tasks SIMOBSERVE and SINANALYSE. We considered the best-fit GALFIT model obtained by fitting the UV continuum. We simulated the same ALMA configuration and integration time used for the actual observation. In Figure A.1 we show the [C II] mock maps imaged with natural and robust (with parameter 1) weights. In both cases imaging is performed with GILDAS.
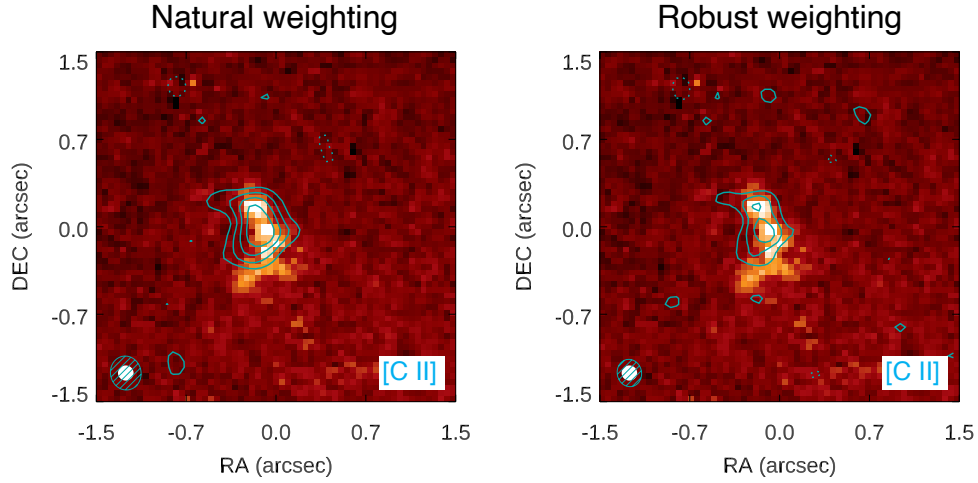

Fig. A.1. Comparison of UV and the [C II] morphology obtained by simulating mock ALMA data for the galaxy image M1. *Left panel*: *HST* UV continuum data (background image) overlaid with the [C II] data obtained with natural weighting (contours). The cyan solid and dashed contours indicate respectively positive and negative levels of 3, 5, 7, 9 rms. The ALMA beam is reported as the cyan ellipse, while the *HST* PSF is reported as the white filled ellipse. *Right panel*: *HST* UV continuum data (background image) overlaid with the [C II] data obtained with robust weighting (contours). Contour levels are the same as in the left panel. Each stamp has a size of $3'' \times 3''$.

Appendix B: Moment maps on the source plane

We created moment maps on the source plane, using the lensing model described in Section 2.2. To create the intensity (moment-0), velocity (moment-1), and velocity dispersion (moment-2) maps, we used the same procedure adopted for the image plane moment maps and described in Section 4.3.
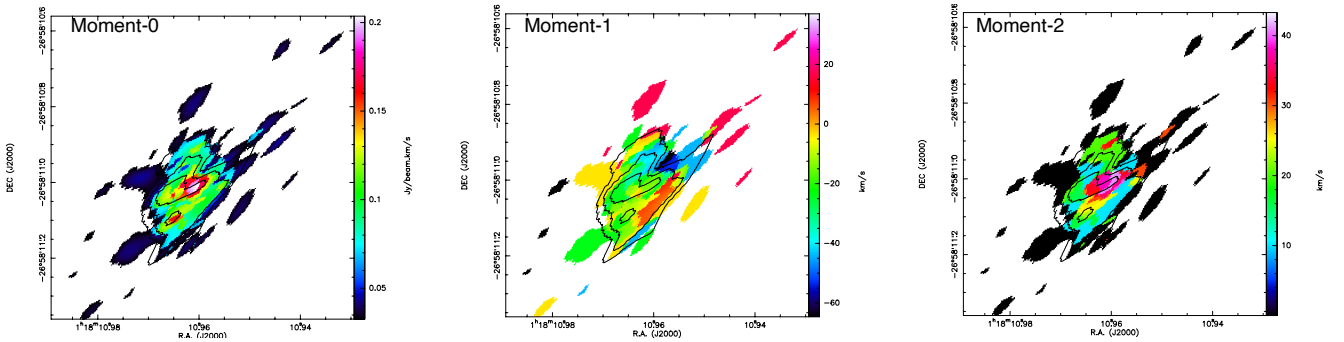
Fig. B.1. Moment maps of our target based on the source plane reconstruction. The symbols are the same as in Figure 6.

Appendix C: Estimates of the [C II] flux of clumps

We estimated the flux of clumps detected in individual channel maps (Section 3.5) using different approaches (Section 3.6). In the following, we briefly describe each method and we report the related measurements in Table C.1.

1. **Image plane.** We fit the [C II] emission in the image plane using customized apertures in each channel, such that they include all the emission above the local rms noise level. For each clump, the line-integrated fluxes were obtained by summing up the flux estimated in each adjacent channel.

2. ***uv* plane, Gaussian.** We fit the [C II] in the *uv* plane using the Fourier Transform of elliptical Gaussian 2D models, in each channel encompassing the emission. The center coordinates, FWHM, and position angle of the Gaussian were free to change in each channel. The total flux was estimated by summing up the fluxes obtained in each adjacent channel.

3. ***uv* plane, PSF free.** We fit the emission in the *uv* plane adopting the Fourier Transform of a 2D PSF model, in each channel. The center coordinates were free to change in each channel. The total flux was estimated by summing up the fluxes obtained in each adjacent channel.

4. ***uv* plane, PSF fixed.** We fit the emission in the *uv* plane with the Fourier Transform of a 2D PSF model, whose coordinates were fixed between different channels (i.e., forced to remain the same in each channel). The total flux was estimated by summing up the fluxes obtained in each adjacent channel.

5. ***uv* plane, PSF fit average.** We fit the average [C II] map in the *uv* plane adopting the Fourier Transform of a 2D PSF model. The maps were obtained by averaging in the *uv* plane (with the GILDAS task uv_average) only the channels encompassing the emission of a given clump.

The fluxes reported in the main text have been estimated adopting method 3.

Table C.1. Observed (i.e., not corrected for magnification) [C II] flux measurements of clumps.

ID	$\mu F_{[C\,II]}$ Image plane (mJy km s^{-1})	$\mu F_{[C\,II]}$ *uv* plane, Gaussian (mJy km s^{-1})	$\mu F_{[C\,II]}$ *uv* plane, PSF free (mJy km s^{-1})	$\mu F_{[C\,II]}$ *uv* plane, PSF fixed (mJy km s^{-1})	$\mu F_{[C\,II]}$ PSF fit average (mJy km s^{-1})	Δv (km s^{-1})
(1)	(2)	(3)	(4)	(5)	(6)	(7)
Clump NE	194 ± 43	174 ± 43	148 ± 36	123 ± 36	104 ± 21	61
Clump SW	291 ± 55	303 ± 66	204 ± 48	121 ± 48	122 ± 23	81
Clump C (tentative)	108 ± 43	113 ± 29	98 ± 24	92 ± 24	93 ± 17	41

Columns: (1) Clump ID; (2) Flux estimated with method 1 described in Appendix C.1; (3) Flux estimated with method 2; (4) Flux estimated with method 3; (5) Flux estimated with method 4; (6) Flux estimated with method 5; (7) Velocity width of the channels encompassing the line emission. Throughout the paper we adopted fluxes estimated using method 3. All methods are described in Appendix C.1.